J. Fluid Mech. (1994), *vol.* 277, *pp.* 163–196

An experimental study of reflected liquefaction shock waves with near-critical downstream states in a test fluid of large molar heat capacity

By SEYFETTIN C. GÜLEN, PHILIP A. THOMPSON AND HUNG-JAI CHO
Rensselaer Polytechnic Institute, Troy, NY 12180-3590, USA

(Received 24 August 1993 and in revised form 13 May 1994)

Near-critical states have been achieved downstream of a liquefaction shock wave, which is a shock reflected from the endwall of a shock tube. Photographs of the shocked test fluid (iso-octane) reveal a rich variety of phase-change phenomena. In addition to the existence of two-phase toroidal rings which have been previously reported, two-phase structures with a striking resemblance to dandelions and orange slices have been frequently observed. A model coupling the flow and nucleation dynamics is introduced to study the two-wave system of shock-induced condensation and the liquefaction shock wave in fluids of large molar heat capacity. In analogy to the one-dimensional Zeldovich–von Neumann–Döring (ZND) model of detonation waves, the leading part of the liquefaction shock wave is a gasdynamic pressure discontinuity ($\Delta \approx 0.1$ μm, $\tau \approx 1$ ns) which supersaturates the test fluid, and the phase transition takes place in the condensation relaxation zone ($\Delta \approx 1$–10^3 μm, $\tau \approx 0.1$–100 μs) via dropwise condensation. At weak to moderate shock strengths, the average lifetime of the metastable state, $\tau \propto 1/J$, is long such that the reaction zone is spatially decoupled from the forerunner shock wave, and J is the homogeneous nucleation rate. With increasing shock strength, a transition in the phase-change mechanism from nucleation and growth to spinodal decomposition is anticipated based on statistical mechanical arguments. In particular, within a complete liquefaction shock the metastable region is entirely bypassed, and the vapour decomposes inside the unstable region. This mechanism of unmixing in which nucleation and growth become one continuous process provides a consistent framework within which the observed irregularities can be explained.

---

1. Introduction

The possibility of complete condensation across a compression shock wave was first shown by Thompson & Sullivan (1975). An adiabatic phase transition from vapour to liquid upon compression is only possible when the slope of the saturated-vapour boundary on a temperature–entropy plane is greater than zero. This is the case for retrograde fluids which have a large number of vibrational degrees of freedom (i.e. large molar heat capacity) so that the work of compression can be stored as internal energy with a correspondingly small increase in temperature. Over the last two decades, extensive shock-tube experiments have been carried out to study retrograde phase-change phenomena. Dettleff *et al.* (1979) produced liquefaction shocks as shocks reflected from the closed end of a shock tube, and verified the existence of shock liquefaction with measurements of pressure, temperature, shock velocity, index of refraction, and photographic observations. Photographs and numerical predictions of liquefaction shock waves emerging from the open end of a shock tube into a large test chamber can be found in Thompson, Carofano & Kim (1986) who also observed a transition from a smooth liquefaction shock front to a chaotic one with increasing shock Mach number. A most unusual form of instability, i.e. numerous tiny vortex rings with two-phase cores, was first observed by Dentleff *et al.* in complete liquefaction shocks. The vortex rings, frequently observed in the experiments described herein, appear to originate in the shock front, move toward it in the frame of downstream liquid, and grow in time to become turbulent. Thompson & Kim (1983) observed that a plane liquefaction shock front emerging from the open end of the shock tube becomes curved and weaker when it is overtaken by the expansion waves originating at the end of the shock tube (e.g. see figures 5 and 6 in Thompson *et al.* 1987*a*) such that three distinct phases, i.e. superheated vapour, metastable vapour, and vapour–liquid mixture, are visible at the corners. Chen, Thompson & Bursik (1986) measured the sound speed of the two-phase liquid–vapour mixture behind the liquefaction shock wave using a simple Mach construction. Comparison with theoretical equilibrium (zero frequency) sound speeds indicated that departures from the equilibrium values increased with increasing shock strength. Using the same method, Thompson *et al.* (1987*b*) measured sound speed in the near-critical states behind a liquefaction shock wave. They found a minimum in the sound speed (≈ 10 m s^{-1}) and the disappearance of two distinct phases at a pressure roughly 25% above the critical value. This surprising discovery initiated the shock-tube experiments presented in this paper, which are intended to enhance our understanding of the non-equilibrium nature of the shock liquefaction and the associated instabilities. A special emphasis is given to complete liquefaction shocks with (calculated) end states in the critical region and near the saturated liquid boundary. A liquefaction-shock model is introduced in §3 to clarify the separate roles played by the dissipative phenomena and the dropwise condensation. The model adequately describes the structure of weak-to-moderate partial liquefaction shocks, and provides new insight into the so-called shock splitting. However, the structure of complete liquefaction shocks appears not to be amenable to a detailed study with classical fluid models.

2. Experimental procedure

Stationary states at high temperatures and pressures in iso-octane are achieved behind a compression shock wave reflected from the shock-tube endwall. Properties of iso-octane are given in table 1. The experimental set-up and the observation chamber are shown in figure 1. Two sections of the shock tube are separated by a diaphragm. A shock wave is created by filling the driver section with nitrogen until the pressure difference across the diaphragm is high enough to rupture it. The shock wave then travels into the stagnant test fluid, and is reflected from the endwall. The x–t diagram of the shock-tube flow is shown in figure 2. The initial (superheated vapour) state 0 is chosen such that the incident shock brings the state very close to the saturation boundary, and liquefaction takes place across the reflected wave.

There is no fundamental difference between liquefaction of a retrograde test fluid across a reflected or an incident shock wave. However, starting from comparable initial states, much higher pressures and temperatures can be achieved behind a reflected wave at lower diaphragm pressure ratios, i.e. lower shock Mach numbers, than behind an incident wave. This in turn ensures complete liquefaction to be achieved at $M_0 < 3$ starting from initial states which can be conveniently maintained in the driven section

Formula	C_8H_{18}
Molecular weight (kg kmol^{-1})	114.23
Boiling point, T_b (K)	372.39
Latent heat at T_b (kJ kg^{-1})	265.0
Critical temperature (K)	543.89
Critical pressure (bar)	25.68
Critical volume (cm^3 g^{-1})	4.10
Pitzer's acentric factor, ω	0.3033
c_v°/R	36.63

TABLE 1. Thermodynamic properties of iso-octane (2,2,4-trimethylpentane)

of the shock tube, i.e. $80 < T_0 < 170$ °C and $0.1 < p_0 < 8$ bar. The advantages of reflected-shock experiments are twofold. First, the fact that the downstream fluid is nominally at rest is desirable for photographic observation. Moreover, the known delay time between the photographed state and the reflection of the incident wave at the endwall gives us information about the characteristic time of the phase transition. The major drawback of the reflected-liquefaction-shock experiments is the interaction of the reflected wave with the boundary layer created by the incident wave which precludes photographic observation from a side window, and distorts the pressure transducer signals.

Pressure jumps across the initial and reflected waves are recorded by the transducers T1–T6 (figure 1*b*) mounted along the test chamber. The pressure and temperature jumps caused by the reflected shock are recorded by the transducers T7 and T8, respectively, mounted at the endwall. The high-frequency acceleration-compensated quartz piezoelectric pressure transducers have 1 μs response time and an accuracy of ±2%. The fast response (0.1 ms), 12.7 μm diameter chromel–constantan thermocouple T8 is of the same design as used by Dettleff *et al.* (1979). The readings of T8 have been corrected using the results obtained by dipping an identical thermocouple into a hot silicon oil bath maintained at a uniform temperature. The test section, which is suspended in the air by Kevlar ropes and covered by 75 mm thick ceramic fibre insulation to prevent heat leakage, is heated by temperature-controlled heating foils. The initial temperature is thus estimated to be maintained within ±1.0 K along the test section. The endwall can be replaced by a 76 mm diameter sapphire window through which photographs of the test fluid downstream of the reflected liquefaction shock wave are taken using a conventional camera (Nikon F3) with open shutters in a dark room. A microflash (0.5 μs flash duration) is used as light source, and it is triggered by the signal of transducer T6 via a delay generator. In the photographs, owing to the scattering, reflection and refraction of the light by the numerous tiny liquid droplets, two-phase regions are easily identified as milky white fog, embedded in a dark background, i.e. a homogeneous single phase. The transient data captured by the pressure and temperature transducers located at the observation chamber walls are recorded by a Nicolet 4094C digital oscilloscope.

For a particular initial state of the test substance, the shock strength is controlled by the thickness of the diaphragm. Repeatability of the experiments, i.e. achieving the same Mach number and downstream state in each experimental run with the same initial state and diaphragm thickness, is important. When a photograph is taken, T_2 and p_2 cannot be measured in the same run because the sapphire window replaces the endwall on which the transducers T7 and T8 are mounted. Therefore, the pressure and temperature defining the thermodynamic state corresponding to an experimental

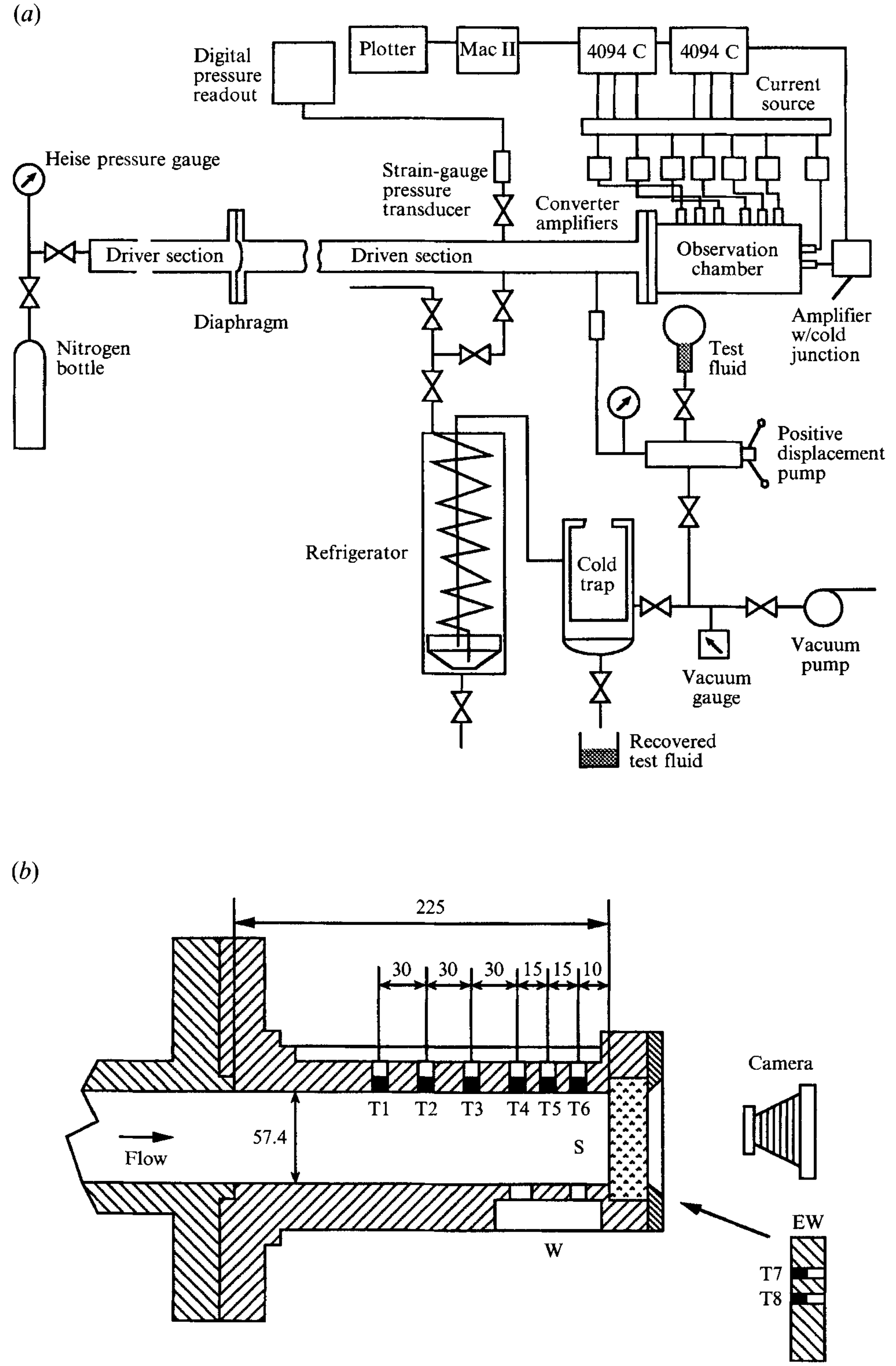

FIGURE 1. (*a*) Schematic diagram of the shock-tube and the measurement system used in the reflected shock experiments. (*b*) Observation chamber. Dimensions in mm. S: sapphire window; W: side window; EW: endwall with transducers.

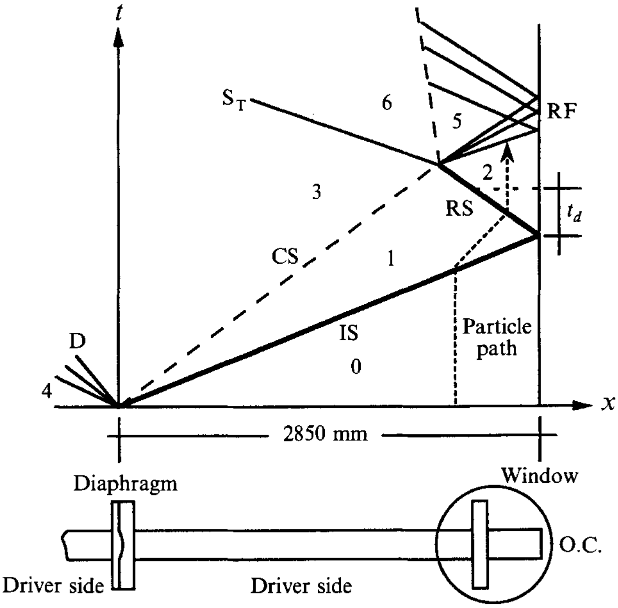

FIGURE 2. x–t diagram of the shock-tube flow. The closed end of the test section is at the right. Arabic numerals designate test fluid states. IS: incident shock; RS: reflected shock; CS: contact surface; D: driver-gas expansion fan; RF: rarefaction fan; S_T: transmitted shock, t_d: delay time. Not to scale.

photograph can be determined from another identical test run with the same initial state and diaphragm. The velocity of the incident shock wave was determined from the known distance between the pressure transducers located at the sidewall and the elapsed time between the signals. The error in determining the incident shock velocity and M_0 is estimated to be within $\pm 3\%$. The velocity of the reflected shock wave was not measured. Repeatability is quite good as far as measurements of pressure and temperature are concerned, and the errors involved are estimated to be less than ± 2–3%.

3. Liquefaction-shock model

A study of the physical mechanisms taking part in the shock-induced condensation in a retrograde fluid is essential for a meaningful interpretation of the experimental results which are presented in §4. A detailed description of the liquefaction shock structure is the subject of a separate paper (Gülen 1993); a compact version can be found in Gülen (1994). An in-depth discussion of the physical models as well as their relevance to the shock-tube experiments performed in the past and to the recent experiments can be found in Gülen (1992). Here, a brief overview will be presented for completeness and convenience as regards the discussion of the experimental findings.

Compression of a retrograde vapour results in condensation which manifests itself in two distinct modes which have been experimentally confirmed. The first mode, as shown in figure 3(*a*), is a two-wave system consisting of a nucleation wave, or the *forerunner shock* (FS), which is a supersonic pressure discontinuity with a superheated (metastable) downstream state. The FS is followed by the so-called *condensation wave* (CD) which is subsonic with respect to the medium separating the two waves. Phase transition from vapour to liquid via dropwise condensation takes place within the CD. Both waves propagate at the same speed in the lab frame, i.e. $u_{CD} = u_{FS}$, assuming a

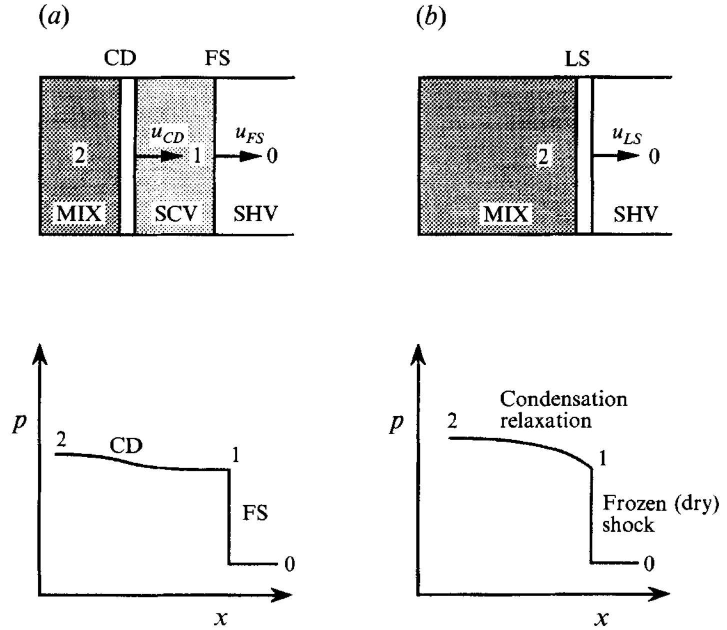

FIGURE 3. Two modes of shock-induced condensation: (*a*) a forerunner shock (FS) followed by a condensation wave (CD), (*b*) a liquefaction shock wave (LS). SHV: superheated vapour; SCV: subcooled (or superheated) vapour which is a metastable state; MIX: equilibrium vapour–liquid mixture.

one-dimensional steady flow. The second mode, the *liquefaction shock wave* (LS), is modelled as a gasdynamic discontinuity with a condensation relaxation zone as shown in figure 3(*b*). The separation between the FS and the CD is controlled by the lifetime of the metastable state τ_{MS}, i.e. $\Delta_{MS} = (u_{FS} - u_{CD})\,\tau_{MS}$, and τ_{MS} is the parameter which controls the transition from a two-wave system to a single relaxing shock wave. Condensation downstream of a liquefaction shock can either be *partial* (i.e. $x > 0$) or *complete* ($x = 0$) depending on the particular initial state and the shock strength.

The energetic characteristics of shock-induced liquefaction of retrograde vapours are determined from the Rankine–Hugoniot (R–H) jump conditions,

$$[h] = \tfrac{1}{2}[p]\,(v_1 + v_0), \tag{1}$$

$$j^2 = \left(\frac{M_0 c_0}{v_0}\right)^2 = -\frac{[p]}{[v]}, \tag{2}$$

$$[p]_i\,[v]_i = [p]_r\,[v]_r, \tag{3}$$

where square brackets denote a jump in the particular property with subscripts 0 and 1 for the upstream and downstream states, respectively. In (2) c_0 is the equilibrium upstream sound speed defined as $(\partial p/\partial \rho)_s^{1/2}$. Equation (2) gives the Rayleigh line (R), and (3) is the condition for shock reflection. A solution to (1)–(3) must satisfy the following conditions for admissibility:

$$[s] > 0, \tag{4}$$

$$j^2 < -\left(\frac{\mathrm{d}p}{\mathrm{d}v}\right)_H = -\frac{\tfrac{1}{2}[p] - c_p/\alpha v}{\tfrac{1}{2}[v] + c_v/(\partial p/\partial T)_v}. \tag{5}$$

Inequality (4) is the second law of thermodynamics, and satisfaction of inequality (5) ensures that the Rayleigh line is always above the adiabat. In (5), $(\mathrm{d}p/\mathrm{d}v)_H < 0$ is the

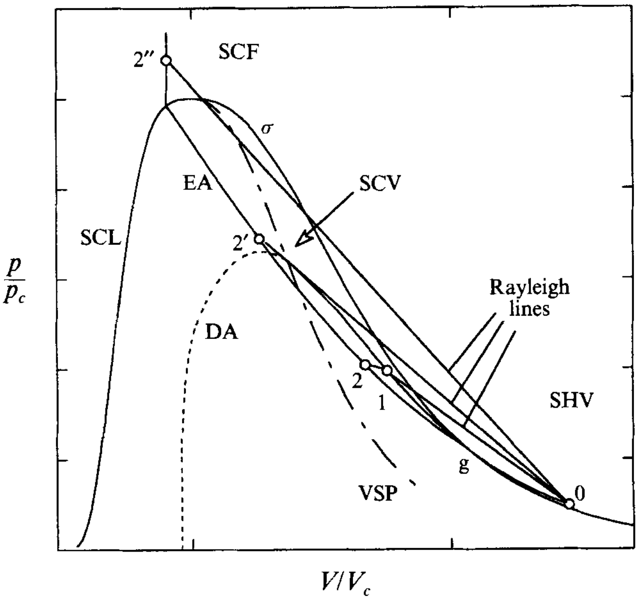

FIGURE 4. Equilibrium (EA) and dry (DA) shock adiabats. SCV: subcooled (supersaturated) vapour, SCL: subcooled (compressed) liquid; SCF: supercritical fluid; VSP: vapour spinodal; σ: coexistence curve; g: intersection of the DA with σ.

slope of the R–H adiabat, and α is the coefficient of volume expansion. The equilibrium adiabat (EA) (see figure 4) is constructed with the assumption that the thermodynamic equilibrium is immediately established in the two-phase region as soon as the saturation boundary (σ) is crossed. There is a kink (g) at the intersection of the EA with σ which is related to the discontinuity in the thermodynamic sound speed at σ. The metastable or dry adiabat (DA) is an extension of the shock adiabat in the superheated-vapour region with the implication that the shock compression is so fast that there is no time for condensation. Note that the horizontal axis in figure 4 is in logarithmic scale in order to preserve the details of the adiabats and the coexistence curve. Since the Rayleigh lines are imposed on the original plot subsequently, the reader should be aware that in a linear-linear plot $0 \rightarrow 1 \rightarrow 2$ is a straight line and $0 \rightarrow 2'$ does not intersect the DA. Although the DA has a branch to the left of the vapour spinodal line (VSP), these unstable downstream states (i.e. $(\partial p/\partial v)_T > 0$) are not admissible in the first place because inequality (5) is not satisfied.

Thermodynamic properties are calculated using a virial-type corresponding-states equation of state,

$$p_r = \frac{1}{Z_c}\left[\frac{T_r}{v_r} + B_2 \frac{T_r}{v_r^2} + \sum_{i=3}^{9} \sum_{j=1}^{9} a_{ij} v_r^{-i} T_r^{2-j}\right], \tag{6}$$

and standard Maxwell relationships. In (6), B_2 is the second virial coefficient by Tsonopoulos (1974), p_r, v_r, and T_r are the reduced pressure, specific volume, and temperature, respectively. For a particular substance with any known three critical parameters, i.e. p_c, v_c, T_c, or Z_c, and the Pitzer's acentric factor ω, the coefficients a_{ij} are determined from a least-squares optimization. Details can be found in Hobbs (1983). The fluid model is completed by the ideal gas correlations for iso-octane by Passut & Danner (1972). Note that a metastable state is a state of partial equilibrium, and it decomposes after a certain time period due to inception of viable nuclei of the more stable liquid phase. There is experimental evidence that the physical properties of the metastable fluid are a smooth continuation of those in the region of stable states; e.g. see Skripov (1992). This enables us to estimate the properties of the supersaturated iso-octane vapour from the metastable portion of the isotherms given by equation (6).

The dissipative structure of the leading shock wave can be modelled by the Navier–Stokes (N–S) equations,

$$p+\dot{q}u-\mu'\frac{\mathrm{d}u}{\mathrm{d}x}=\dot{q}u_1+p_1, \tag{7}$$

$$\dot{q}(h+\tfrac{1}{2}u^2)-\mu' u\frac{\mathrm{d}u}{\mathrm{d}x}-\kappa\frac{\mathrm{d}T}{\mathrm{d}x}=\dot{q}(h_1+\tfrac{1}{2}u_1^2), \tag{8}$$

where $\dot{q}$ is the mass flow rate per unit area, $\mu'=\frac{4}{3}\mu+\mu_b$ with shear and bulk viscosities μ and μ_b, respectively, and κ is the conductivity. From (7) and (8), with $\mu_b=2\mu$, the characteristic thickness and time of the nucleation wave are calculated to be 0.1 μm and 1 ns, respectively. For heavy molecules such as iso-octane, it is reasonable to expect that the vibrational relaxation time will be of the order of $\tau_v\approx 10^{-10}$ s or even less (Dremin 1992). Hence, τ_v is of the same order as the relaxation times for rotational and translational modes. Considering that in molecules with more than 10 atoms the energy states of a harmonic oscillator lie very close to each other, i.e. effectively forming a continuous band, it can be concluded that the vibrational–translational energy transfer in such molecules is significantly enhanced. Thus, in a shock transition zone in iso-octane, the relaxation mechanisms of all three degrees of freedom of internal molecular energy are strongly coupled so that μ_b in the N–S equations must account for the rotational and vibrational non-equilibrium.

The dropwise nucleation model describes non-equilibrium condensation as the creation of critical nuclei in a supersaturated vapour and their subsequent growth. From statistical mechanical considerations, the nucleation rate J can be expressed as

$$J=\Phi q_c\beta A^*Zc_1\exp(-\Delta G^*/kT). \tag{9}$$

For an in-depth discussion of the homogeneous nucleation concept, the reader can consult the excellent article by Feder *et al.* (1966). In (9), $\beta=p/(2\pi mkT)^{1/2}$ is the collision frequency of vapour molecules on the unit surface of a cluster, A^* is the surface area of a critical cluster of radius r^*, Z is the non-equilibrium factor of Zeldovich, and c_1 is the concentration of monomers (molecules). The non-isothermal correction factor Φ accounts for the heating of the nuclei by molecules impinging on it, and the mass-accommodation factor q_c accounts for the fact that some molecules are reflected from the cluster surface. Different nucleation models are in general of the same form as (9), but they differ in their formulation of the nucleation activation barrier, ΔG^*. In this work, we use a homogeneous nucleation model which is based on a semiphenomenological droplet model for the Helmholtz free energy of the clusters; e.g. see Dillmann & Meier (1991), Delale & Meier (1993). This model contains the translational, rotational, vibrational, and configurational contributions to the droplet free energy in addition to the surface tension (considered alone in the classical capillary model).

In an actual flow where pressure and temperature both change with time, the actual nucleation rate $J(t)$ is found from

$$\frac{\mathrm{d}J}{\mathrm{d}t}=\frac{J_s(p,T)-J}{\tau_n(p,T)}, \tag{10}$$

where $$\tau_n(p, T) = (2\pi \Phi q_c \beta A^* Z^2)^{-1} \tag{11}$$

can be considered as a local relaxation time. J_s is the steady-state nucleation rate given by (9) which can only be reached at infinite time when all transient effects have disappeared from the system. At low Mach numbers $\tau_n \gg \tau_{FS}$, so that the nucleation lags the forerunner shock. With increasing M_0, τ_n approaches τ_{FS} and (9) gives a good estimate of the actual time-dependent nucleation rate.

Critical clusters which are formed within the nucleation wave at a rate given by (9) grow further by molecules impinging on the cluster surface. The droplet growth rate is estimated by

$$\frac{\mathrm{d}r}{\mathrm{d}t} = C\frac{\kappa(1-r/r^*)}{L\rho_l r}[T_s(p)-T''] = C\frac{\kappa}{L\rho_l r}[T'-T''], \tag{12}$$

where $T_s(p)$ is the saturation temperature corresponding to the pressure of the vapour phase, L is the latent heat of condensation, ρ_l is the density of the condensate, and superscripts $''$ and $'$ denote vapour and liquid phases, respectively. Detailed derivation of (12) can be found in Young (1982). The factor C contains $Pr = \mu c_p/\kappa$, $Kn = \lambda/2r^*$, specific heat ratio γ, q_c, gas constant R, $T_s(p)$, and L, with the rigid-sphere mean-free-path $\lambda = 1.5\mu(RT)^{1/2}/p$ which in this case should be interpreted as a characteristic molecular length. Typically, $\lambda \approx O(10\ \text{Å})$, and an equivalent molecular diameter for the iso-octane molecule is estimated to be $d \approx 8$ Å. Note that (12) covers the free-molecular ($Kn \gg 1$), continuum ($Kn \ll 1$), and the so-called slip ($Kn \approx 1$) flow regimes. When $Kn \approx O(1)$, in the immediate vicinity of the droplet ($\Delta r \approx O(\lambda)$) a free-molecular regime is assumed, whereas continuum theory is applicable in the far field.

Within the condensation discontinuity, or the phase-change relaxation zone of the liquefaction shock front, non-equilibrium condensation dominates the dissipative phenomena. For a one-dimensional steady flow in the constant-area shock tube, with the approximations of no-slip and negligible volumetric fraction of the liquid phase, the continuity, momentum, and energy equations are

$$\frac{\rho'' u}{1-y} = \dot{q}, \tag{13}$$

$$\frac{\mathrm{d}p}{\mathrm{d}x} + \frac{\rho'' u}{1-y}\frac{\mathrm{d}u}{\mathrm{d}x} = 0, \tag{14}$$

$$\frac{\mathrm{d}h''}{\mathrm{d}x} - \frac{1}{\rho''}\frac{\mathrm{d}p}{\mathrm{d}x} + \frac{[h_g(T')-h''(T'')-L(T')]}{1-y}\frac{\mathrm{d}y}{\mathrm{d}x} + \frac{y}{1-y}c_{p,l}(T')\frac{\mathrm{d}T'}{\mathrm{d}x} = 0. \tag{15}$$

The wetness fraction is given as

$$y(x) = \frac{4\pi\rho_l}{3\dot{q}}\int_{x_0}^{x} r^3(x,\xi)\,J(\xi)\,\mathrm{d}\xi \tag{16}$$

at x due to (i) the creation of critical-size nuclei at x, and (ii) the growth of nuclei born at ξ and observed at x, where $x_0 < \xi < x$, and x_0 is the point at which the state of the vapour is the theoretical saturation value (i.e. $S = 1$). In (15), $c_{p,l}(T')$ is the liquid specific heat, and $h_g(T')$ is the enthalpy of the saturated vapour at the droplet surface as distinct from the enthalpy of the vapour in the far field. The derivation of (13)–(16), and the solution method is described in detail in Gülen (1992).

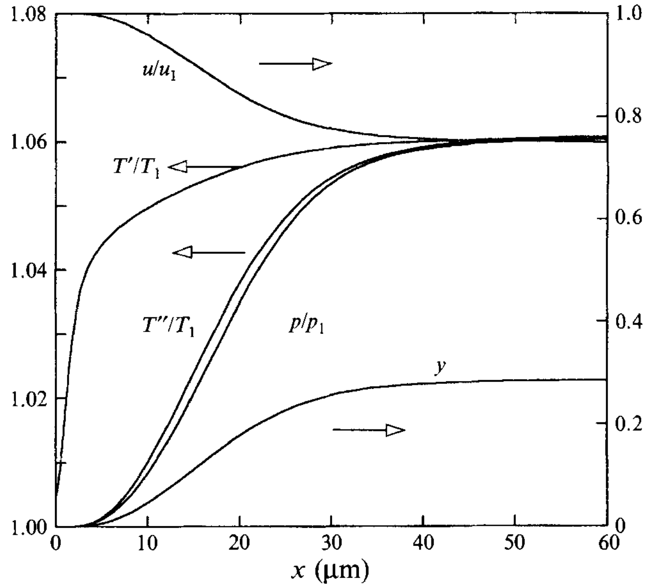

FIGURE 5. Pressure, particle velocity (in the shock frame), temperature, and wetness fraction variation in the condensation zone. $p_0 = 0.402$ bar, $T_0 = 100$ °C, $M_0 = 2.0$. Subscript 1 denotes the metastable state downstream of the forerunner shock; $p_1 = 5.79$ bar, $T_1 = 153.4$ °C, $u_1 = 76.4$ m s^{-1}.

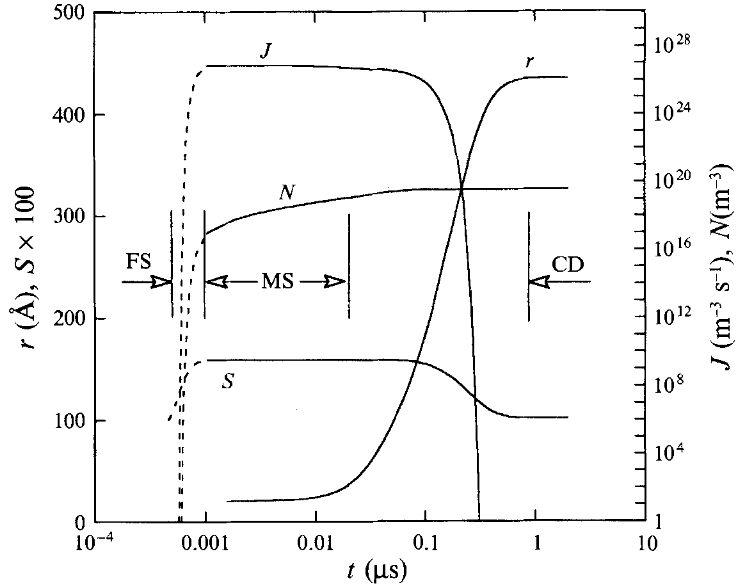

FIGURE 6. Nucleation rate J, supersaturation S, average droplet radius r and droplet number density N across the liquefaction shock wave. $p_0 = 0.402$ bar, $T_0 = 100$ °C, $M_0 = 2.0$.

Typical results can be found in figures 5 and 6 and in table 2. The CD is a fully dispersed subsonic (with respect to the fluid downstream of the FS) wave with relaxation mechanisms associated with mass, momentum, and heat transfers between liquid droplets and vapour. Far from the critical point, the mass transfer between the phases is controlled by the molecular kinetics, i.e. the impact and absorption of vapour

M_0	S	$N\,(\mathrm{m}^{-3})$	$\log J$	τ_n (ns)	τ_{ms} (ns)	τ_{CD} (μs)	Δ_{CD} (μm)	r (Å)	y (%)
1.9	1.50	4×10^{16}	22.6	8.0	167	133.0	2850	3706	23
2.0	1.59	4×10^{19}	26.9	4.4	62	2.0	27	435	29
2.1	1.67	2×10^{21}	29.4	2.6	16	0.14	3	114	33

TABLE 2. Condensation parameters: supersaturation S; average droplet number density N, nucleation rate $J\,(\mathrm{m}^{-3}\,\mathrm{s}^{-1})$; nucleation lag time τ_n; characteristic time and length of the CD, τ_{CD} and Δ_{CD}, respectively; lifetime of the metastable state τ_{MS}; average droplet radius at the end of condensation r; wetness fraction y. $p_0 = 0.402$ bar, $T_0 = 100$ °C

M_0	n^*	r^* (Å)	λ (Å)	δ (Å)
1.8	277	28	57	23
2.0	73	18	41	20
2.2	32	14	32	17

TABLE 3. Radius of the critical cluster r^*, average number of molecules per critical cluster n^*, molecular mean free path λ, and average intermolecular distance δ. $p_0 = 0.402$ bar, $T_0 = 100$ °C

molecules upon the droplet surface. The droplet temperature relaxation is very rapid, and the momentum relaxation is neglected (no-slip condition), which is a reasonable assumption due to small droplet sizes. Hence, the characteristic time of the condensation zone, τ_{CD}, is mainly controlled by the thermal relaxation process. In essence, increasing shock strength, which leads to increasing supersaturation and nucleation rates, results in faster condensation and finer droplets with higher number densities. One should note that at the requisite densities in the metastable-vapour region, iso-octane molecules are interacting almost continuously as illustrated by table 3 where $\delta = (\rho/m)^{-1/3}$ is the average intermolecular spacing. The parameters in table 3 suggest that the droplets are nucleated in the slip regime, and they grow in the continuum regime. The reader may compare the values in table 3 to typical values of r^* and λ in the expansion of moist air in nozzles and wind tunnels, i.e. 5–6 Å and 1000 Å, respectively.

The expansion of a regular fluid such as steam inside a nozzle cannot result in supersaturation beyond a certain limit which is referred to as the *Wilson* point. This is mainly a direct effect of the latent heat released by the nucleated clusters which leads to a pressure rise, thus neutralizing the pressure gradient of the flow. Further condensation via droplet growth diminishes supersaturation and restores the thermodynamic equilibrium. The resulting pressure increase is commonly referred to as the condensation shock, which is a somewhat misleading term because the flow is supersonic throughout the entire process. The Wilson line is the actual (kinetic) limit of metastability where supersaturation and nucleation rate both reach a maximum. Experiments show that it is well before the vapour spinodal line, which is the absolute boundary separating metastable and unstable states. However, inside a liquefaction shock region, the pressure rise due to the latent heat of cluster formation and the shock pressure gradient are both positive. In this case, determination of a Wilson point is rather arbitrary; it boils down to a single question: What is the limiting mass fraction of the liquid droplet which signals the onset of condensation? Although there is no single correct answer to this question, earliest detection of light scattering by the microscopic droplets in experimental studies usually corresponds to $10^{-3} > y > 10^{-4}$ which can be considered as the location of the Wilson point (Wu, Wegener & Stein

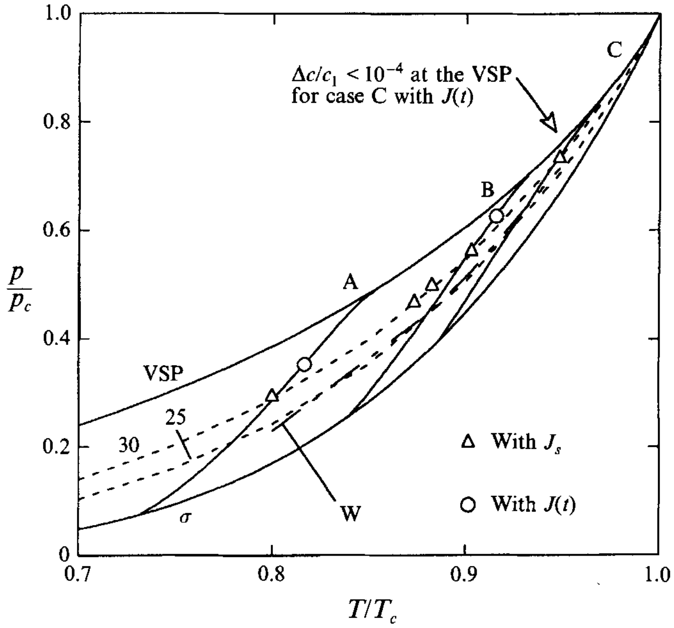

FIGURE 7. State points corresponding to $\Delta c/c_1 = 10^{-4}$, the lines of constant J, and the (metastable) reflected adiabats. W: Wilson line; 30: $J = 10^{30}$ m^{-3} s^{-1}; 25: $J = 10^{25}$ m^{-3} s^{-1}.

1977). One can estimate the depletion of molecules via nucleation within the leading shock zone as

$$\Delta c(t) = \int_{t_0}^{t}\left(\int_{t'}^{t}\frac{\mathrm{d}n}{\mathrm{d}\tau}\mathrm{d}\tau + n^*(t')\right)J(t')\,\mathrm{d}t' \approx \int_{t_0}^{t} n^*(t')\,J(t')\,\mathrm{d}t', \tag{17}$$

where n^* is the number of molecules in a critical cluster (Feder *et al.* 1966). The growth rate of the cluster size, $\mathrm{d}n/\mathrm{d}t$, has a negligible contribution during the rapid forerunner shock transition. For low moisture contents, y and $\Delta c/c_1$ are roughly identical, and (17) can be integrated decoupled from the N–S equations to estimate the monomer depletion. Figure 7 shows points corresponding to $y \approx \Delta c/c_1 = 10^{-4}$ on the DA for different initial states which are coincident with the line of $J = 10^{30}$ m^{-3} s^{-1}. As long as $\Delta c/c_1 < 10^{-4}$ within the shock zone ($t \sim 1$ ns), the fluid can be expected to be shocked to a near-spinodal state or to an unstable state. As can be seen in figure 7, accounting for the time delay of nucleation pushes the actual (kinetic) limit of metastability to the vapour spinodal (VSP). Also shown in figure 7 is a *pseudo*-Wilson line which was identified by Thompson *et al.* (1987*a*) as the upper limit of shock splitting based on erroneous arguments.

The weakest link in the model presented herein is the surface tension, which appears in the exponential term in (9) and strongly affects the calculated nucleation rates. In our calculations we use a corresponding-states formula (Reid, Prausnitz & Poling 1989) which agrees with the available data in the normal liquid range. However, this is no guarantee for the reliability of the surface tension values used herein at high temperatures near the critical point. Fortunately, this is not as severe an impediment as it first appears to be. The qualitative predictions of the model are not affected by the changes in J due to the uncertainties in the parameters such as surface tension used in (9). The only effect is a shift in the Mach number at which, say, transition from two-wave condensation to a single shock takes place. This can be remedied by introducing

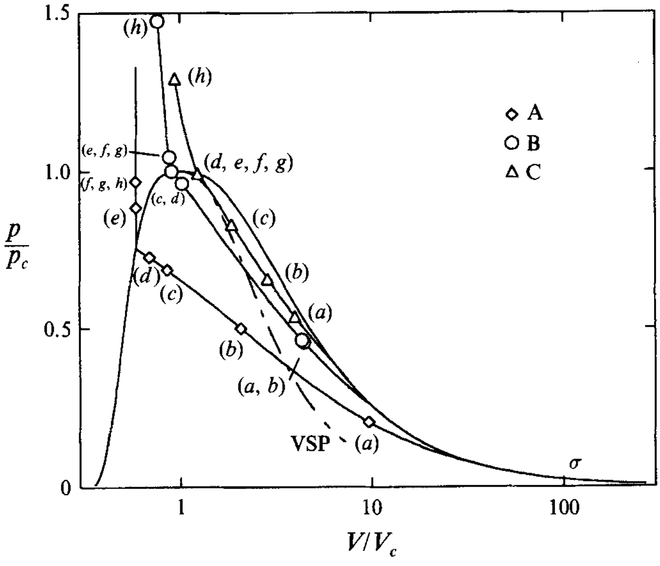

FIGURE 8. Equilibrium reflected-shock adiabats. The points shown correspond to the experimental photographs shown in figures 17–19, and the parameters for A, B and C are given in table 4.

	A	B	C
p_0 (bar)	0.402	0.445	0.457
T_0 (°C)	100	130	140
v_0 cm^3 g^{-1})†	661.6	648.0	647.3
c_0 (m s^{-1})†	164.6	171.4	173.7
M_g	1.47	1.97	2.19
M_s	2.44	2.58	2.70
M_l	2.71	2.82	††

TABLE 4. Initial pressure and temperature of iso-octane in the test section corresponding to the equilibrium adiabats shown in figure 8. M_g and M_l correspond to the intersection of the EA with the saturated vapour and liquid boundaries. M_s corresponds to the intersection of the DA with the VSP. † Calculated using the state equation (6), from the measured p_0 and T_0. †† The EA intersects the saturated vapour boundary at $M_0 = 2.80$

a 'fudge factor' into the exponential term in (9) such that experimentally observed range of Mach numbers are reproduced. This point is discussed in detail in Gülen (1993).

4. Experimental results

Representative results of the reflected-liquefaction-shock experiments in iso-octane are summarized here. A more comprehensive description of the visual and quantitative data can be found in Cho (1990). The three different initial states which have been used in the majority of the shock-tube experiments are given in table 4. The corresponding equilibrium Hugoniot adiabats are shown in figure 8, and the points refer to the experimental pictures shown in figures 17–19.

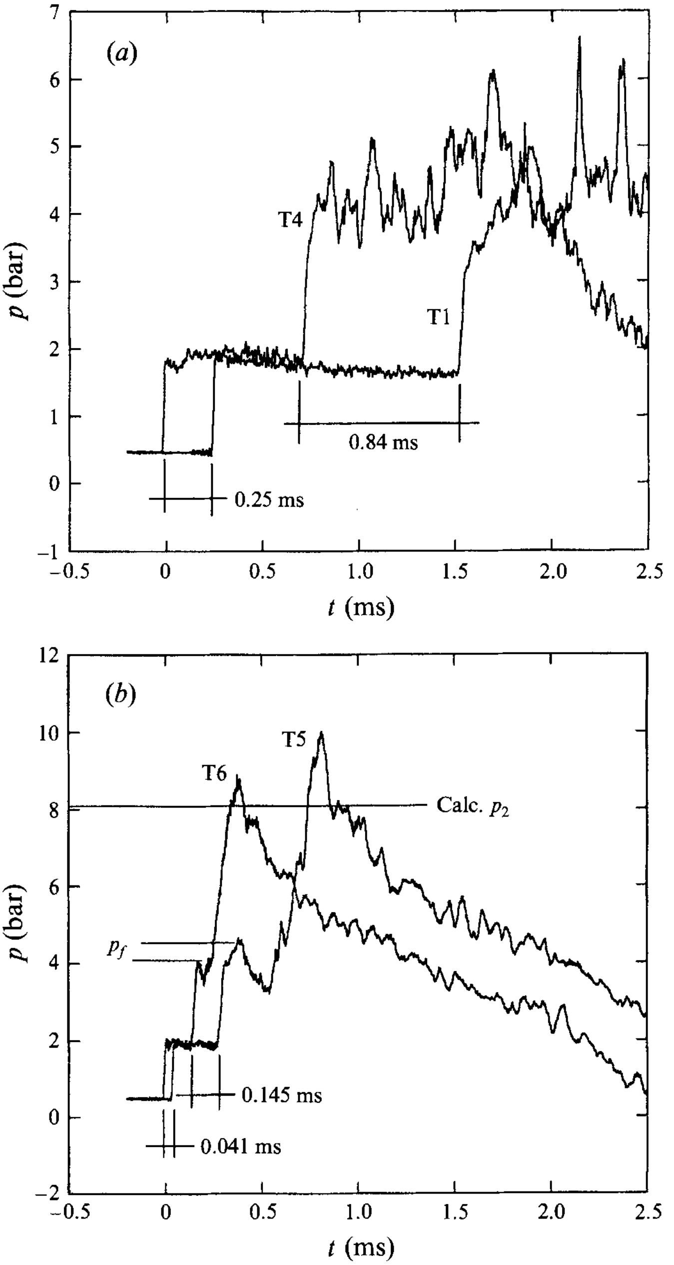

FIGURE 9(a,b). For caption see facing page.

4.1. *Measurements*

Figure 9(a–d) shows the pressure and temperature histories recorded by the transducers mounted at the side- and endwalls of the test chamber for the experiment #oct042690-2 which is representative of the majority of the experiments with end states in the two-phase region. The consecutive pressure jumps caused by the incident and reflected shocks and recorded by transducers T1, T4, T5, and T6 are shown in figure 9(a, b). The pressure p_1 downstream of the incident shock can be obtained (as an average) from pressure traces T1–T6 rather accurately, and p_1 as a function of M_0 is shown in figure

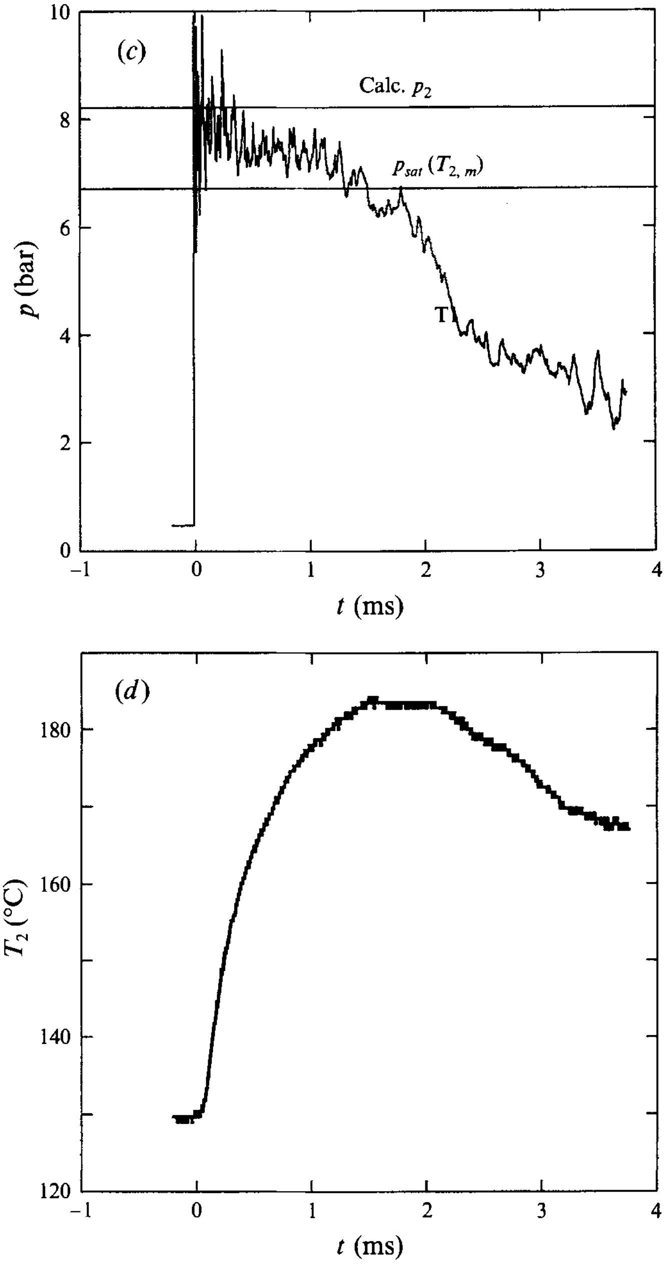

FIGURE 9. (*a*) Transient pressures from T1 and T4; (*b*) transient pressure from T5 and T6 (p_f is the pressure under the bifurcated foot of the reflected wave shown in figure 11); (*c*) transient pressure from transducer T7 (measured temperature, $T_{2,m}$ = 183.4 °C); (*d*) transient temperature recording of T8. Test run #oct042690-2; $p_0 = 0.445$ bar, $T_0 = 130$ °C, $M_0 \approx 2.08$. Calculated values are $p_2 =$ 8.2 bar, $T_2 = 195.8$ °C.

10. When several experiments are carried out with the same diaphagm and initial state (p_0, T_0), the average M_0 and p_1 are plotted, with error bars representing the standard deviation as an estimate of the accuracy. Within the experimental accuracy, the agreement between the measured pressures and those calculated using the equilibrium R–H model is reasonably good.

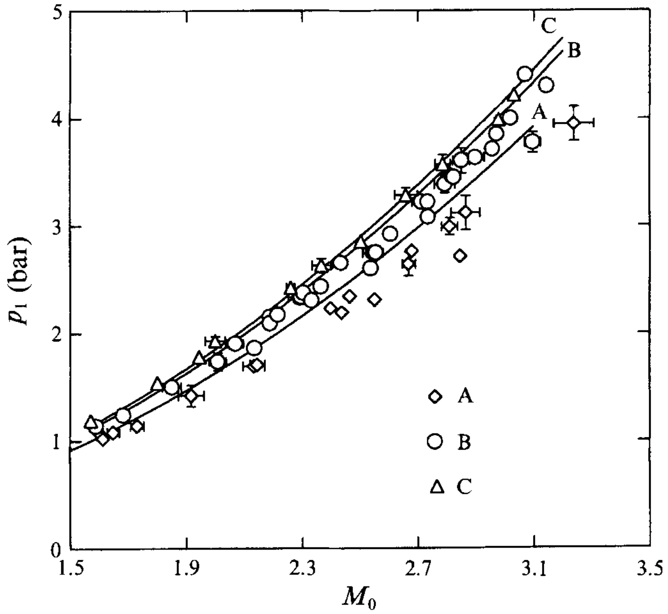

FIGURE 10. Measured pressures downstream of the incident shock wave (no condensation). (For A, B, C see table 4.)

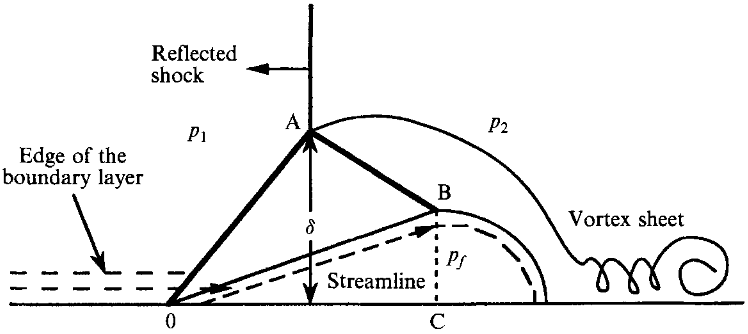

FIGURE 11. Schematic diagram of the bifurcated foot of the reflected shock wave (after Strehlow & Cohen 1958).

Although pressure recordings of the transducers T1–T6 are suitable for reliable measurements of u_{IS} and p_1, they can not be used for the measurement of u_{RS} and p_2 owing to the interaction of the reflected shock wave with the boundary layer created by the incident wave. From figure 9(*a*, *b*), u_{RS} is estimated to be 105.3 m s^{-1} compared to a calculated value of 70 m s^{-1}, and the reflected wave appears to accelerate, which is a physical impossibility. The two-step pressure jump recorded by transducers T5 and T6 (signalling the arrival of the reflected wave) is caused by the bifurcation of the reflected (liquefaction) shock wave as shown in figure 11. The boundary-layer flow, unable to pass under the reflected shock into the downstream region, separates and gathers in a growing bubble which is carried along under the reflected shock. An oblique shock then precedes the normal reflected shock, and a second oblique shock develops between the intersection of the front leg, the main shock and the upper surface of the fluid ball. Thus, the initial pressure jump indicates the arrival of the first oblique

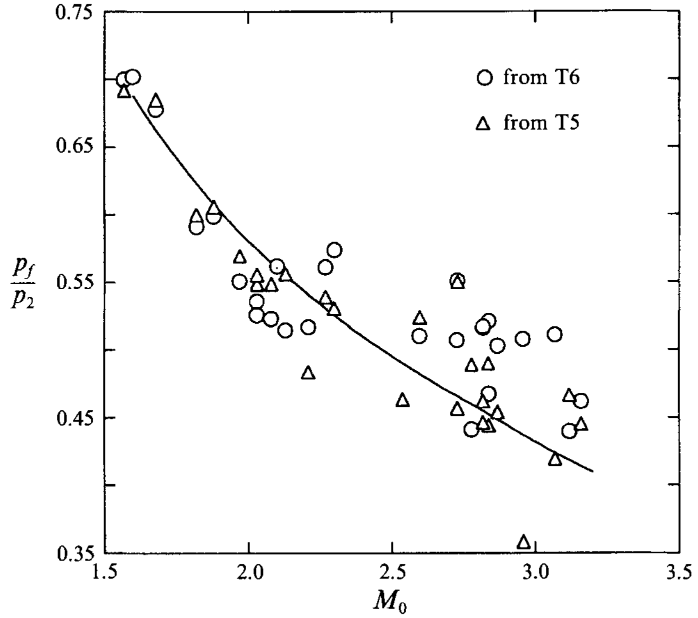

FIGURE 12. Pressure p_f under the bifurcated foot of the reflected shock wave. The solid line represents $(p_1/p_2)^{0.4}$ calculated from the R–H jump conditions.

shock, which travels faster than the normal reflected shock, followed by the subsequent gradual rise. Strong real-gas effects and phase change across the reflected wave make a quantitative analysis of shock bifurcation in our experiments extremely difficult. Strehlow & Cohen (1958) found that the bifurcation and acceleration of the reflected shocks were extremely severe in polyatomic gases with low values of γ, even at moderate shock Mach numbers, and the bifurcated foot quickly filled the shock tube. Indeed, this effect can be easily seen in the pressure traces recorded by the transducers T1 and T4 which are located 100 and 40 mm away from the endwall, respectively. In experiments performed with nitrogen, Davies & Wilson (1969) found that $p_f/p_2 = (p_1/p_2)^{0.4}$ for Mach numbers less than about 2.5 which approximately agrees with the pressure recordings T5 and T6 as shown in figure 12.

A reliable measurement of p_2, the downstream pressure behind the normal reflected shock wave, free from the bifurcation effects can be obtained from transducer T7 mounted at the endwall. Figure 13 shows p_2 values obtained from recordings of T7 as a function of M_0 for three sets of experiments. As shown in figure 9(*c*), the arrival of the incident shock at the endwall is signalled by the sudden jump in the pressure signal of T7, followed by a plateau indicating a uniform state 2 conforming to the ideal one-dimensional reflected-shock behaviour. Upon the interaction of the reflected shock wave with the contact surface (CS), a shock is transmitted into region 3 and a rarefaction wave (RF) is reflected into region 2 (see figure 2). The arrival of the RF is signalled by the drop in the T7 pressure signal. The data points in figure 13 correspond to the pressure plateau following the initial jump recorded by T7. Within the accuracy of the measurements, there is good agreement between measured and calculated pressures.

Temperature T_2 behind the reflected liquefaction shock wave is measured by the thermocouple T8. As can be seen in figure 9(*d*), the T8 signal has a longer rise time than the signals of the pressure transducers. The T_2 data in figure 14 correspond to the

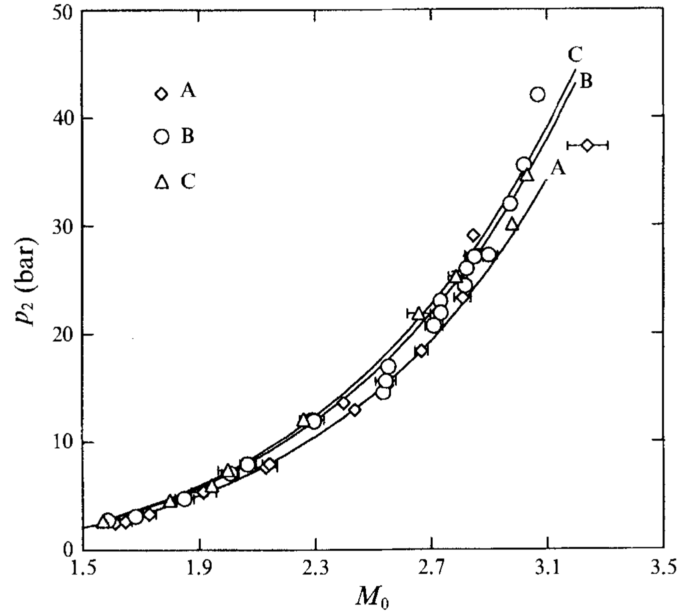

FIGURE 13. Measured pressures downstream of the reflected liquefaction shock wave.

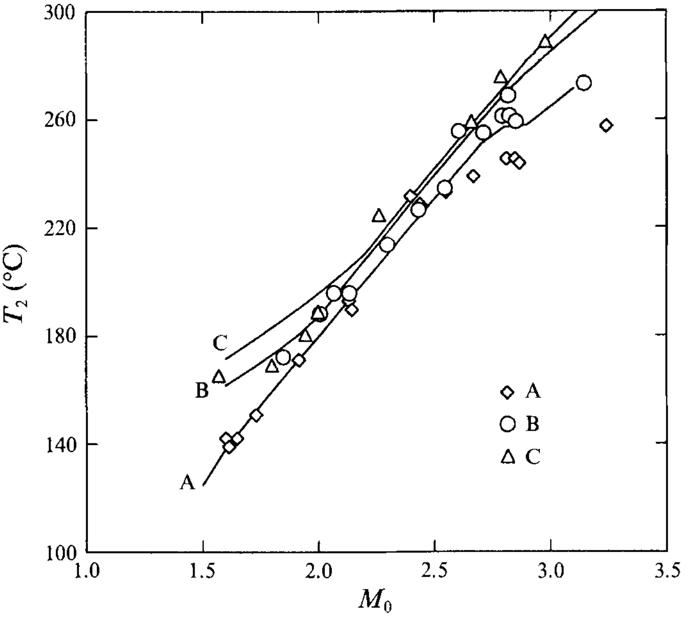

FIGURE 14. Measured temperatures downstream of the reflected liquefaction shock wave.

maximum of the signal of T8, corrected as mentioned in §2. Note that the time constant of T8 (0.1 ms) is much higher than τ_{CD} at higher Mach numbers. The measured temperatures are consistently lower than the values predicted by the equilibrium R–H model by 5–20 K for complete liquefaction shocks. This deviation, also observed in experiments by Dettleff *et al.* (1979), cannot be attributed to a defect in the thermocouple, and it is usually well outside the estimated experimental uncertainty of

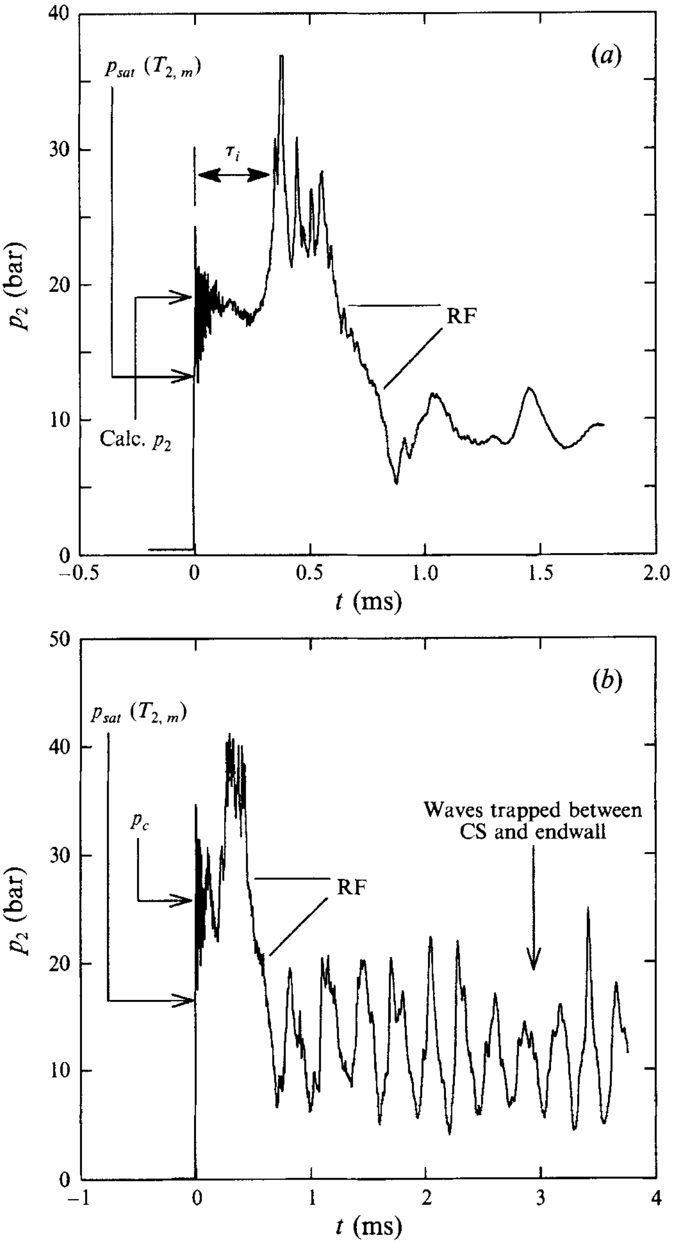

FIGURE 15. (*a*) Transient pressure from T7. Test run #oct041290-4; $p_0 = 0.402$ bar, $T_0 = 100$ °C, $M_0 \approx 2.70$. Calculated values are $p_2 = 19$ bar, $T_2 = 250$ °C. Measured temperature, $T_{2,m} = 223$ °C. (*b*) Transient pressure from T7. Test run #oct062790-1; $p_0 = 0.445$ bar, $T_0 = 130$ °C, $M_0 \approx 2.83$. Calculated values are $p_2 = 25.9$ bar, $T_2 = 271.4$ °C. Measured temperature, $T_{2,m} = 241.2$ °C.

±2%. A possible source for this is the inaccuracy of the equation of state in the compressed-liquid region. However, it is more likely that the gradual rise in T_2 is closely associated with relaxation to equilibrium.

The pressure histories in figure 15, recorded by T7 for two experiments with different initial states, clearly show successive jumps in pressure. This type of signal has been consistently observed in complete and partial-liquefaction-shock experiments. From

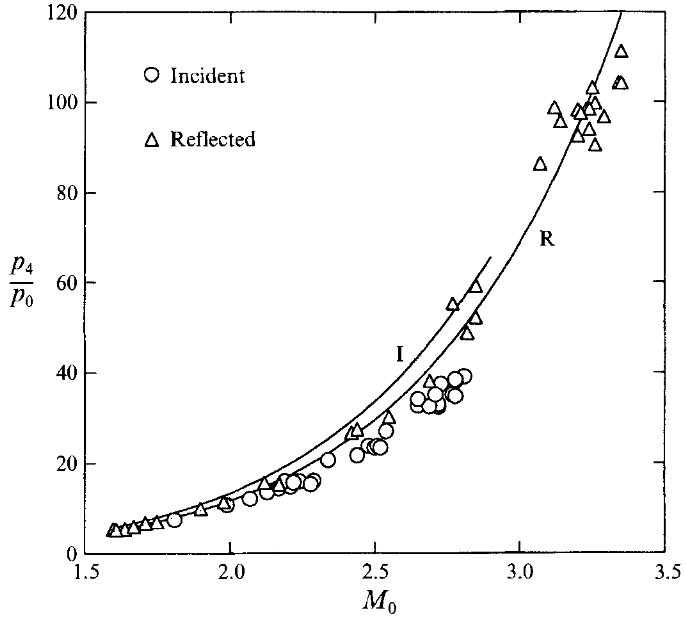

FIGURE 16. Diaphragm pressure ratio as a function of incident (I) and reflected (R) liquefaction-shock experiments in iso-octane.

figure 15, the first jump and the following plateau, usually of a duration of less than 0.5 ms, is roughly in agreement with p_2 calculated with the equilibrium R–H model. The subsequent jump in pressure, although somewhat less steep than the first one, is significant in magnitude, and it forms a second plateau with large oscillations before the RF arrives. The RF subsequently reflects between the wall and the CS, and the type of the reflected wave alternates between a rarefaction and a shock. Thus, the pressure and temperature of the iso-octane trapped between the wall and the CS fall after the passage of the RF, and then rise and fall to a lesser extent with the subsequent weaker reflected disturbances. The frequency and the amplitude of the pressure oscillations in figure 15(*b*) are higher than those in figure 15(*a*) because, for near-critical states in region 2, rarefaction changes the fluid state to superheated vapour which has a higher sound speed and acoustic impedance, ρc. In contrast, when states in region 2 are liquid or two-phase fluid with $y \approx 1.0$, the state after the rarefaction is still two-phase with considerably lower sound speed and acoustic impedance.

The ideal-shock calculations in §3 are based on one-dimensional steady flow in a shock-fixed frame with instantaneous diaphragm removal. Strictly speaking, a shock wave created by a diaphragm burst never reaches a true steady state, but it travels a certain distance before it reaches a maximum speed and starts to decelerate gradually. Figure 16 shows the experimental and calculated diaphragm pressure ratio p_4/p_0 as a function of M_0 for incident and reflected liquefaction shocks. For a given shock Mach number M_0 and the initial state (p_0, T_0) the equilibrium downstream pressure p_1 and particle velocity u_1 are calculated using the R–H model. Matching the pressure and velocity across the contact surface, i.e. $p_1 = p_3$ and $u_1 = u_3$, the Riemann equation

$$u_3 = -\int_{\rho_3}^{\rho_4} c\frac{d\rho}{\rho} = -\int_{T_3}^{T_4}\left[\frac{c_p(T)\,c_v(T)}{RT}\right]^{1/2} dT, \tag{18}$$

is used to calculate p_4. In both cases the driver gas is nitrogen, and the temperature of

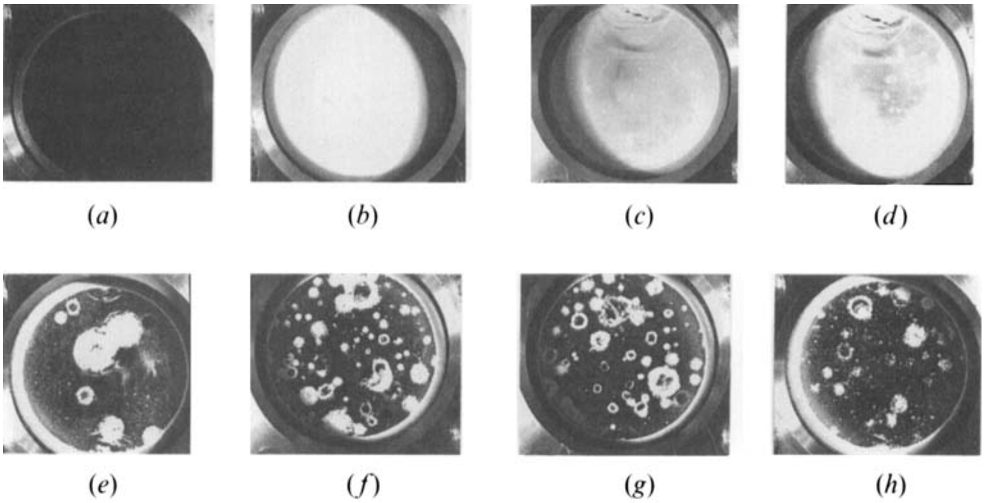

(*a*) (*b*) (*c*) (*d*)

(*e*) (*f*) (*g*) (*h*)

FIGURE 17. Photographs of iso-octane behind the reflected (liquefaction) shock wave; $p_0 = 0.402$ bar, $T_0 = 100$ °C.

	(*a*)	(*b*)	(*c*)	(*d*)
test run #	oct051290-2	oct051290-5	oct051390-2	oct051490-1
M_0	1.92	2.46	2.64	2.68
t_a(μs)	18.4	19.4	20.0	20.3
	(*e*)	(*f*)	(*g*)	(*h*)
test run #	oct051490-2	oct051590-5	oct051590-3	oct051490-3
M_0	2.81	2.87	2.87	2.87
t_a(μs)	20.0	8.7	6.0	20.3

the nitrogen prior to the diaphragm rupture is taken to be equal to the room temperature, $T_3 = 25$ °C. The calculated and measured diaphragm pressure ratios in figure 16 agree well in the reflected-shock case whereas the discrepancy for the incident-shock case indicates that for a given p_4/p_0 the measured M_0 is significantly higher than that predicted by the ideal R–H and Riemann models. White (1958) showed that the pressure waves resulting from the mixing of the driver and driven gases at the contact surface would increase the shock strength if the heat capacity of the driver gas were less than the heat capacity of the driven gas, i.e. $c_{p,nitro} \ll c_{p,iso}$, so that the shock wave would require even larger distances to reach the maximum Mach number. The effect of mixing at the contact surface on the shock strength is expected to be especially significant in the case of an incident liquefaction shock wave with a two-phase downstream state because c_p will tend to very large values, and the shock wave will still be accelerating when it reaches the end of the relatively short driven section of the shock tube. In comparison, the state downstream of the incident shock wave in a reflected-liquefaction-shock experiment is still superheated vapour, and the driven section of the tube is almost twice as long as the old one (50 *vs.* 29 shock-tube diameters) so that the incident wave has enough time to reach its maximum strength. For example, from figure 9(*a*, *b*), $u_{IS} = 360.0$ m s^{-1} between T1 and T4, and $u_{IS} = 365.9$ m s^{-1} between T5 and T6 such that the difference between the two is within the accuracy of determining the shock speed, which is ±3% or 11 m s^{-1} in this case (i.e. $M_0 = 2.12 \pm 0.06$).

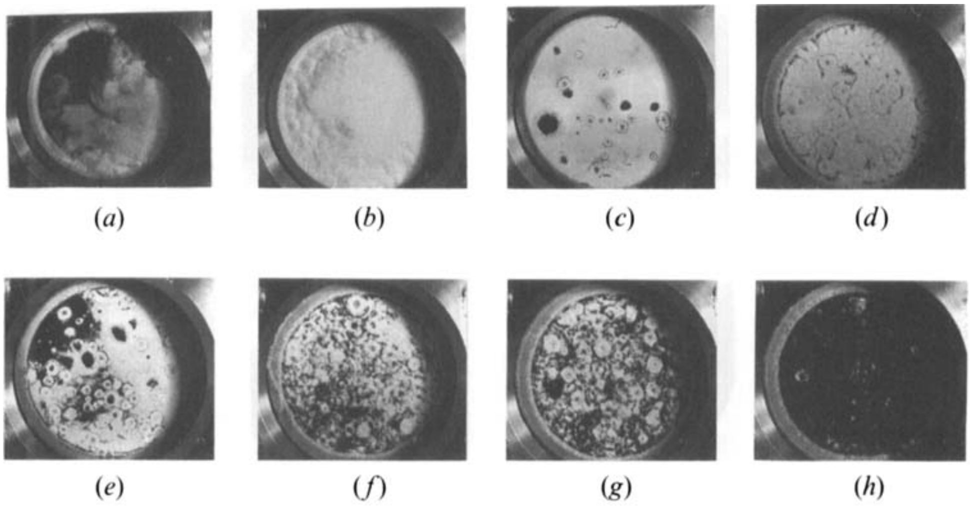

FIGURE 18. Photographs of iso-octane behind the reflected (liquefaction) shock wave; $p_0 = 0.445$ bar, $T_0 = 130$ °C.

	(a)	(b)	(c)	(d)
test run #	oct050390-4	oct042990-5	oct050490-6	oct050190-2
M_0	2.29	2.30	2.79	2.79
$t_d(\mu s)$	29.7	30.7	4.4	29.0

	(e)	(f)	(g)	(h)
test run #	oct050490-5	oct050190-1	oct043090-3	oct043090-4
M_0	2.82	2.82	2.85	3.10
$t_d(\mu s)$	14.3	29.7	29.3	30.0

4.2. *Photographic observations*

A major part of this study is extensive photographic observation of the states behind the reflected liquefaction shock wave through sapphire window mounted at the end of the shock tube. Figures 17–19 show a selection of photographs taken in three series of experiments in the order of increasing incident shock Mach number M_0, and the corresponding states on the equilibrium reflected adiabats are shown in figure 8. The thickness of the shocked fluid layer between the reflected shock and the endwall is roughly 0.5–2 mm, depending on the delay time and the shock speed. A careful examination of the experimental pictures, and comparison with detailed calculations reveal the existence of several distinct phase-change phenomena which are discussed below.

For low shock Mach numbers, photographs do not reveal the existence of the liquid phase behind the reflected shock wave although equilibrium calculations indicate a two-phase downstream state. As discussed in §3, a shock compression initially supersaturates the vapour to an intermediate metastable state, and condensation occurs subsequently via nucleation and droplet growth. However, if the shock is weak and the supersaturation is low, the nucleation rate may not be enough to start the condensation within the observation time, and the downstream state is supersaturated vapour. For instance, there is no visible condensation in figure 17(*a*), which shows the test fluid behind the reflected wave ($M_{RS} = 1.76$) 18.4 μs after the incident shock wave ($M_0 = 1.86$) is reflected from the endwall. For this particular initial state and shock strength, the nucleation rate is calculated as $J = 7.8 \times 10^{19}\ \mathrm{m}^{-3}\ \mathrm{s}^{-1}$ corresponding to a supersaturation $S = 1.46$. The thickness and the timescale of the condensation zone are

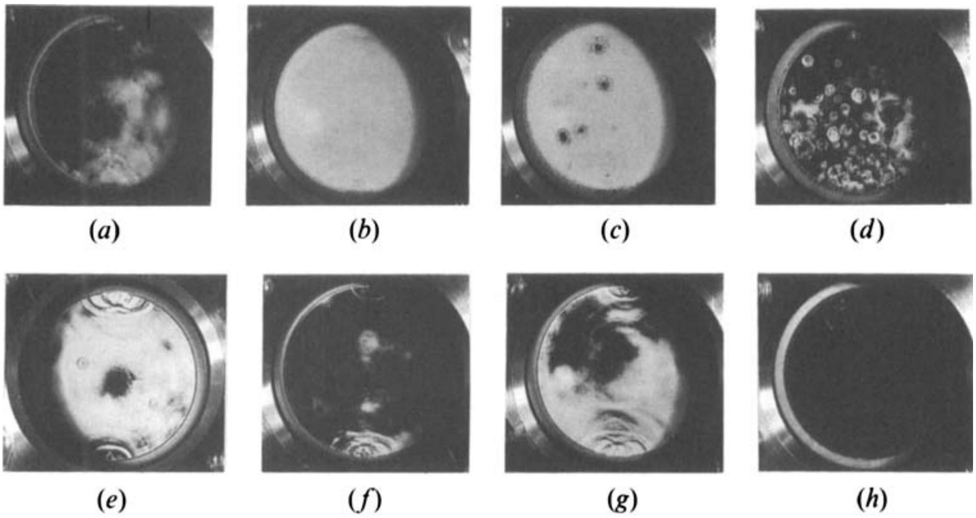

(a) (b) (c) (d)

(e) (f) (g) (h)

FIGURE 19. Photographs of iso-octane behind the reflected (liquefaction) shock wave; $p_0 = 0.457$ bar, $T_0 = 140$ °C.

	(a)	(b)	(c)	(d)
test run #	oct052390-4	oct052390-1	oct052290-2	oct052290-3
M_0	2.37	2.50	2.66	2.79
t_d(μs)	19.3	20.0	20.7	20.3
	(e)	(f)	(g)	(h)
test run #	oct052490-1	oct052490-3	oct052490-2	oct052290-4
M_0	2.79	2.79	2.79	2.98
t_d(μs)	10.4	2.7	5.3	19.7

calculated to be $\Delta_{CD} \approx 35$ mm and $\tau_{CD} \approx 1.6$ ms, respectively ($\tau_{FS} \approx 1$ ns). Therefore, it is clear that no appreciable condensation will be observed because $\tau_{CD} \gg 18.4$ μs. According to the calculated CD structure, the wetness fraction at $t = 18.4$ μs is $y \approx 0$ as compared to the final wetness fraction $y = 0.204$.

The iso-octane which is used in the experiments has a minimum purity of 99.9%, and the impurities are limited to the isomers of C_8H_{18} so that the heterogeneous nucleation effects which may arise from the presence of nucleation centres are negligible. However, since the wall temperature remains close to the initial temperature T_0 throughout the experiment, the fluid adjacent to the wall is compressed almost isothermally thus reaching saturation well before the bulk fluid so that a thin fog layer is formed at the shock-tube wall. This effect is enhanced by the fact that the wall provides a large wetting surface for heterogeneous nucleation. Nevertheless, it is safe to say that the primary mechanism of condensation in the bulk fluid downstream of the plane shock wave is homogeneous nucleation. The fog layer due to early condensation at the shock tube wall can be readily seen in figures 17–19.

At higher Mach numbers, supersaturation is high enough that the nucleation rate reaches a value sufficient to start the condensation within the observation time. The liquid phase thus formed consists of a large number of tiny droplets evenly distributed in the vapour. Owing to the scattering, reflection and/or refraction of the light by these liquid droplets, a two-phase downstream state appear in the photographs as a milky-white fog layer which completely or partially fills the shock tube. Ideally, as long as the end state is a two-phase mixture, one would always expect to see a homogeneous and smooth white fog layer filling the entire tube (figures 17*b*, 19*b*). However, turbulent

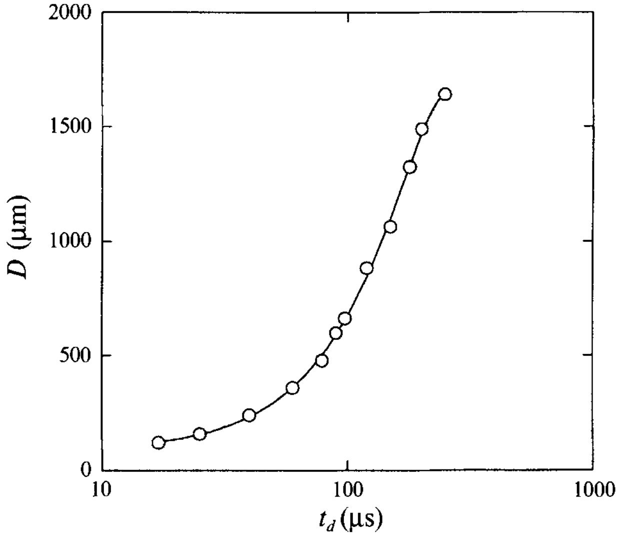

FIGURE 20. The average outer diameter of the two-phase vortex rings from experimental pictures which are taken with increasing delay times ($p_0 = 0.402$ bar, $T_0 = 100$ °C).

cloud-like two-phase mixtures (figure 18*b*) which partially or completely fill the tube, circular two-phase structures with a small core and either a surrounding ring or radially aligned elongated beams have been frequently observed especially in experimental sets B and C (figures 18*a*, 19*a*). The appearance of these irregularities is perplexing to say the least, and we were unable to account for their formation in a satisfactory way. For the case shown in figure 18(*b*), the nucleation rate is calculated to be $J = 4.2 \times 10^{26}$ m^{-3} s^{-1} ($S = 1.19$) with a condensation-zone thickness of $\Delta_{CD} \approx$ 36 µm and $\tau_{CD} \approx 1.8$ µs, which is considerably less than $\tau_d = 30.7$ µs. The average droplet radius at the end of condensation zone is estimated as $r \approx 538$ Å with an average droplet number density of 2.9×10^{16} m^{-3}. In order to have an idea about the calculated average droplet size, consider that the wavelength of the visible light in the electromagnetic spectrum is of the order of 5×10^3 Å, and the mean free path in the surrounding vapour at the downstream state is estimated as 27 Å from the rigid-sphere model.

For complete liquefaction shocks, photographs consistently show the existence of toroidal configurations with two-phase cores. There are several indications (outlined in detail by Dettleff *et al.* 1979 who first discovered their existence) which suggest that these are vortex rings. In the compressed liquid region, these vortex rings have sharply defined two-phase cores (figure 17*e*–*h*). Although it is difficult to determine their initial size from photographs, the visible rings have diameters of tens of µm and higher (see figure 23). Once these rings are born (in or behind the liquefaction shock front) they tend to grow with time, decaying and/or merging in the process to form larger rings and conglomerates of rings. The growth rate of the outer diameter of visible rings obtained from experimental photographs is illustrated by the plot in figure 20. In figure 17(*c*, *d*) one can still see small rings behind a fog of relatively lower droplet number density than in figure 17(*b*). This is somewhat puzzling because the R–H downstream state for the latter has a lower moisture content. It seems that with increasing shock strength liquefaction needs longer times, which contradicts the results in table 2. In the near-critical region, the rings are larger with more diffuse two-phase cores with several smaller and more sharply defined rings still discernible in between (figure 18*f*, *g*). Of particular interest are photographs showing gaping round holes (i.e. a homogeneous single phase) and a number of relatively large rings embedded in a fog layer which completely or partially fills the tube (figure 18*c*, *e*, also figure 19*c*). These unique observations are typical of the reflected shock experiments (B) for $M_0 = 2.78$–2.84 which, within the error of measurement, approximately correspond to the immediate proximity of the critical point on the equilibrium reflected-shock adiabat. Increasing shock strength results in supercritical fluid states downstream of the liquefaction shocks, and vortex rings are observed even at $M_0 \approx 3.10$ ($p_2 \approx 1.4p_c$); e.g. see figure 18(*h*). The vortex rings were still visible in very strong shocks with resulting downstream pressures as high as $1.8p_c$.

In addition to small vortex rings, peculiar two-phase regions with a striking resemblance to orange slices or dandelions are also observed in the experimental set C at Mach numbers corresponding to the intersection of the EA with the saturated vapour boundary near the critical point, i.e. $M_0 \approx 2.80$ (figure 19*d*, *e*, *g*). According to the equilibrium R–H model, the dandelions and vortex rings observed in experimental sets B and C correspond to thermodynamic states within the critical region (i.e. $T \approx T_c \pm 0.03T_c$, $\rho \approx \rho_c \pm 0.25\rho_c$). The diffuse boundaries of these irregular two-phase structures (as compared to the sharply defined rings in the compressed liquid region) may be an indication of the increasingly large liquid–vapour interface in the vicinity of the critical point. This, of course, brings us to the question of how close we really are to the critical point. Figure 14 shows that the measured temperatures are 5–10 K below the calculated values. In the reflected-shock experiments (B), for $M_0 \approx 2.80$ the equilibrium R–H model predicts that temperature and pressure downstream of the RS are approximately equal to the critical values, i.e. 25.3 bar and 543 K. Considering that the measured pressures agree with the R–H predictions (figure 13) and accounting for the temperature deviation, the downstream state may very well be within the critical region, but it may not be close enough to the critical point in order to observe the near-critical anomalies. There are also other factors which make it difficult to estimate the proximity of the shocked state to the critical point in each experimental run, e.g. the measurement errors and the accuracy of the temperature control. However, it is reasonable to expect that a few among a large number of identical experimental runs with the same initial state and diaphragm should indeed shock the test fluid to a near-critical state.

5. Discussion

Examining the adiabat system in figure 4 reveals that the Rayleigh line does not intersect the dry adiabat for complete liquefaction ($0 \rightarrow 2''$) or for strong partial liquefaction ($0 \rightarrow 2'$). Physically, however, a shock wave must have a finite inner structure governed by the dissipative and phase-change phenomena. Thus, in the absence of a metastable intermediate state, the physical model in §3 (i.e. the wave systems in figure 3) is rendered useless. Two possibilities emerge: (i) the occurrence of unstable wave fronts, and (ii) a transition from a nucleation and growth to a spinodal phase-change mechanism. A third possibility is that, for sufficiently strong shocks such that the downstream state is supercritical fluid, the intermediate states within the shock transition zone may be entirely outside the two-phase region (figure 19*h*). Thompson *et al.* (1986) reported chaotic shock fronts which were observed in experiments with test fluids FC75 and PP3. Our calculations for these fluids and the relevant initial conditions show that chaotic shock fronts correspond to an intersection of the R with the EA without an intersection with the DA in the metastable region. Unfortunately,

M_0	$\Delta c/c_1$	Δp_{FS} (bar)	Δp_L (bar)
2.0	8.0×10^{-8}	4.2	4.5×10^{-6}
2.1	1.3×10^{-5}	5.2	9.2×10^{-4}
2.2	3.1×10^{-4}	6.3	2.7×10^{-2}

TABLE 5. Mass fraction of condensed phase $y \approx \Delta c/c_1$, R–H pressure jump Δp_{FS}, and pressure increase due to latent heat release Δp_L within the nucleation zone of the reflected liquefaction shock wave. $p_0 = 0.402$ bar, $T_0 = 100$ °C

there is no adequate theory to predict the absolute limit of mechanical stability of the LS front. However, it is extremely unlikely that stable shock fronts exist beyond a monomer depletion level of $\Delta c/c_1 = 10^{-4}$ (i.e. $y = 10^{-4}$). In order to support this claim, consider the pressure increase due to heat released by the nucleated clusters within the nucleation wave (or the nucleation zone of the LS), i.e.

$$\Delta p_L \approx \frac{\dot{q}L}{u}\frac{\Delta c}{c_1}. \tag{19}$$

Calculated values of Δp_L is given in table 5. At low Mach numbers, perturbations caused by the inhomogeneities (clusters) which are formed inside the shock front ($\Delta p_L \approx 10^{-6}$ bar) will be quite small. It is quite conceivable that these perturbations and the transverse waves which corrugate the LS front are closely related. At higher Mach numbers, Δp_L becomes of the order of tens of millibars and higher such that the partial LS front becomes fully unstable with a striking resemblance to a cumulus cloud. In passing we should mention the similarity between these liquefaction-shock-front disturbances and detonation instabilities (Shepherd, Thompson & Cho 1990). There is a strong likelihood that similar instability mechanisms are at work, considering the analogy between the wave models and the non-equilibrium parameters, i.e. the moisture content and the extent of chemical reaction, both of which can be represented by an Arrhenius-type equation. There is ample experimental evidence that the LS front instability is closely associated with the phase transition mechanism. In particular, a connection between the absence of a metastable state predicted by the R–H model and the observed irregularities is unmistakable. As can be seen in figure 21 for $M_0 > 2.66$ and initial state C, the Rayleigh line intersects the EA before the DA. Experimental photographs for that particular initial state and the range of M_0 consistently reveal the existence of irregular two-phase structures (cf. figures 8 and 19*d*–*g*). Figure 6 in Thompson *et al.* (1987*b*) shows a plane (undistorted) complete LS emerging from the driven section of the shock tube into the observation chamber with numerous vortex rings clearly visible within or behind the shock front. We tend to believe that the metastable region is entirely bypassed inside a complete LS transition zone. In that case the supersaturated fluid decomposes spontaneously in the unstable region bounded by the vapour and liquid spinodal lines. This will be elaborated in the following paragraphs.

5.1. *Near-spinodal states and spinodal decomposition*

Spinodal decomposition (SD) and dropwise condensation are two mechanisms for vapour to liquid phase transitions in a single-component fluid. The original theory of spinodal decomposition treats the critical nucleus of the new phase as a fluctuation in density; e.g. see Cahn (1968), Skripov & Skripov (1979). At low supersaturations inside the metastable region, the critical nucleus can be considered as a droplet separated by a sharp interface from the surrounding vapour. This, however, is the premise which the

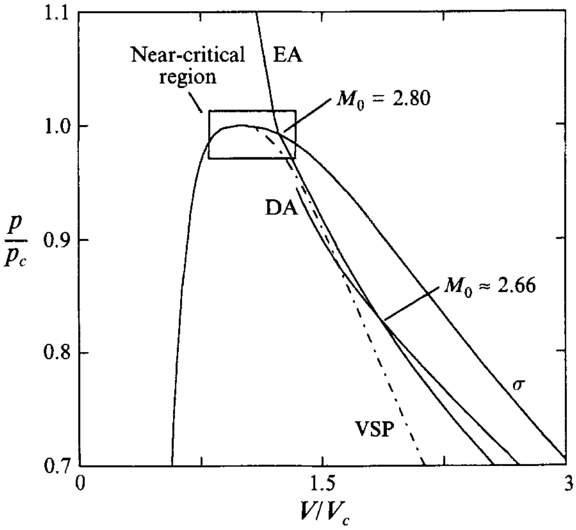

FIGURE 21. Equilibrium and dry adiabats near the critical point. $p_0 = 0.457$ bar, $T_0 = 140$ °C.

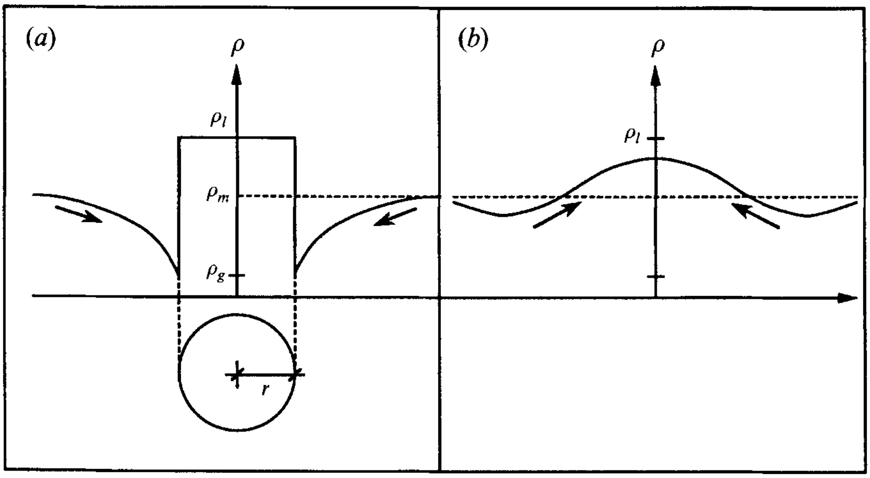

FIGURE 22. (*a*) Density variation for a liquid droplet of radius r and density ρ_l in a superheated vapour of density ρ_g (homogeneous nucleation); (*b*) instantaneous density variation near the spinodal due to molecular fluctuations.

well-known homogeneous nucleation theory is based upon. The difference between the two types of clustering mechanisms is shown in figure 22. Critical droplets can grow further by capturing the impinging molecules to complete the phase transition. With increasing penetration into the metastable region, the fluctuations increase such that the critical nucleus cannot be approximated as a homogeneous droplet with the density of the bulk liquid phase. The phase transition at or beyond the limit of the metastability, i.e. the spinodal line, is via a diffusive flux of molecules against the density gradients. Therefore, homogeneous nucleation and spinodal decomposition form the two limits of a fundamental phase transition process. At one end, clusters formed by random molecular fluctuations grow via molecular kinetics whereas at the other end nucleation and growth take place simultaneously. Spinodal decomposition was initially observed in binary liquid mixtures where a sample was quenched from a supercritical temperature into the unstable region bounded by the spinodal lines. The characteristic features are the continuous change in the composition of the phases and the resulting interconnected two-phase morphology. Spinodal decomposition is also encountered in rapid phase transitions from a stable supercritical state to a thermodynamically unstable state below the critical temperature in a single-component fluid. The telltale sign of SD in that case is the light-scattering rings observed in the experiments; e.g. see Schmitz, Klein & Woermann (1993). The physical phenomena discussed herein differ from those observations in that the phase transition is driven by a pressure jump and proceeds across the metastable region.

Experimental photographs clearly show that initially microscopic vortex rings are formed in or behind the liquefaction shock front. These rings grow with time, decaying and/or merging in the process to form larger rings and conglomerates of rings and ultimately a two-phase fog filling the entire tube. The initial absence of a homogeneous droplet cloud suggests that the usual phase-change mechanism of dropwise condensation has either been bypassed or degenerated into some other mechanism. We offer a tentative explanation for the formation of the toroidal two-phase structures based on the assumption that the phase transition is facilitated by spinodal decomposition. It should be kept in mind that, at the requisite densities, the molecules of a retrograde vapour (supersaturated or superheated) interact almost continuously (see table 3). This is significant because the distinction between liquid and vapour phases of a pure fluid is quantitative (i.e. the degree of interaction between the molecules) rather than qualitative. Inside the leading-shock zone, the phase boundary is traversed and the test fluid is supersaturated rapidly leading to the formation of microscopic nuclei ($r \approx O(10\ \text{Å})$). These nuclei, however, are not sufficient in number and do not have time to grow to result in any significant condensation. Meanwhile, the molecular fluctuations rise to such a level that spontaneous density gradients are formed across the entire volume of the fluid. These regions of higher molecular density grow and connect with each other by diffusive flux of molecules to form the new phase. The clusters (i.e. nuclei) which have been formed earlier act as centres from which a density gradient spreads. Hydrodynamically, the dense regions of the fluid are accelerated to a lesser extent by the pressure gradient than the lighter regions. This is expected to produce vorticity around the regions of lower average density which will be transformed into a torus-like structure due to vortex roll-up. Scattering of light by microscopic droplets (clusters) inside the vortex ring core results in the smoke-ring-like appearance. The short-range equilibrium between the molecules is established rapidly within the shock front forming the liquid phase (dark regions in the pictures). For a characteristic length of $l \approx \delta \approx r$ (see table 3), the timescale can be estimated as $\tau \approx l^2/D \approx 10^{-11}$ s with the diffusion coefficient, $D \approx 10^{-7}\ \mathrm{m^2\ s^{-1}}$.

In quenching of binary alloys, the phase separation characteristically starts with the formation of clusters (i.e. composition gradients) which are initially uniformly dispersed across the matrix, and then grow (coarsen) via *negative* diffusion, i.e. against the gradient in composition, into distinct regions of coexisting equilibrium phases. The coarsening is increasingly slow because the diffusion has to proceed across larger and larger distances. Photographs of the shocked test fluid downstream of the reflected wave taken with a Questar microscope reveal that the vortex rings have a characteristic size and spacing of the order of 10 μm (figure 23). The characteristic time for a cluster to diffuse over a distance l and coalesce with its neighbour is approximately $\tau_D \approx l^2/D \approx 1$ ms. This can be considered as a characteristic time for the conglomeration of the two-phase rings which is in good agreement with the experiments; e.g. in figure 20 of Dettleff *et al.* (1979) the time between the first occurrence of the ring vortices and

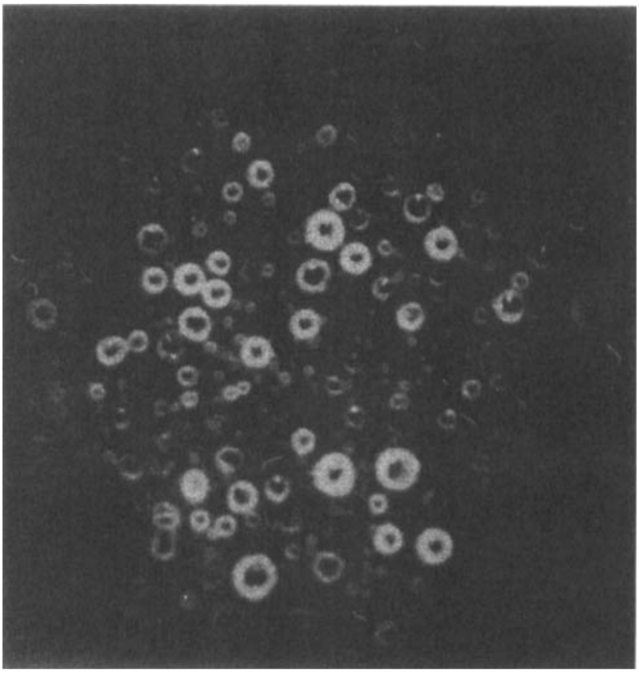

FIGURE 23. Photograph of iso-octane downstream of the reflected LS taken with Questar microscope (25 × magnification). Test run #oct080791, $p_0 = 0.474$ bar, $T_0 = 100$ °C, $M_0 = 2.90$, $t_a = 26$ μs.

the final fog filling the entire tube is approximately 1.4 ms. The diffusion rate in the retrograde test fluids at the requisite densities and temperatures is much larger than in solids, e.g. roughly 10^{-7} m^2 s^{-1} as compared to 10^{-13} m^2 s^{-1} for a solid near the melting point, so that the vortex rings coalesce completely into a uniform fog in contrast to the final coarse and grainy matrix observed in crystalline systems.

5.2. *Near-critical states*

Near the critical point (CP), the mean-square density fluctuations given as

$$\langle \Delta\rho^2 \rangle = \frac{1}{V} kT\rho^2 \kappa_T, \tag{20}$$

where $\kappa_T = (\partial\rho/\partial p)_T/\rho$ is the isothermal compressibility, become increasingly large. The observed non-analytic character of the thermodynamic behaviour near the critical point is associated with long-range density fluctuations in the fluid system, and the physical properties primarily depend on a single variable, i.e. the so-called correlation length ξ. When the density fluctuations given by (20) become of the order of $(\rho_f - \rho_g)^2$, a spontaneous phase transition is possible, i.e. for a fluid volume of V

$$V \approx \xi^3 \approx \frac{kT\rho^2\kappa_T}{(\rho_f - \rho_g)^2}, \tag{21}$$

so that ξ gives us a measure of the lengthscale of the mean effective range of density fluctuations. Experiments carried out along the critical isochore for $T > T_c$ for several substances resulted in the power law $\xi = N\epsilon^{-\nu}$ Å, where $\epsilon = 1 - T_r$, $N = 1.25$–3.64 and $\nu = 0.61$–0.63 (Jany 1988). For iso-octane, from (21) with the equation of state (6), we estimate

$$\xi = 1.22\epsilon^{-0.614} \text{ Å} \tag{22}$$

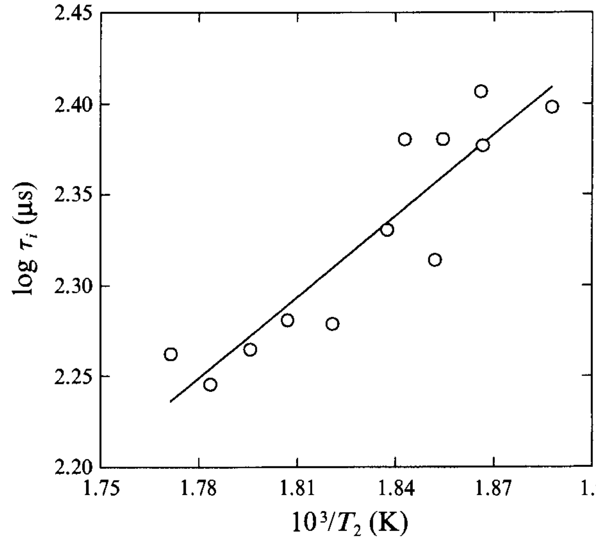

FIGURE 24. Time delay between the consecutive pressure jumps recorded by T7 (cf. figure 15). $p_0 = 0.445$ bar, $T_0 = 130$ °C.

on the path $\rho = \rho_g$. A characteristic time for a fluid volume of V to reach equilibrium near the CP can be given as $\tau_\xi = \xi^2/D_T$ such that, using (22) with the thermal diffusivity $D_T \approx 10^{-7}$ cm^2 s^{-1}, we find that $\tau_\xi \approx 1.5|\epsilon|^{-1.23}$ ns. In order to have an idea about the magnitude of τ_ξ, consider that for $\Delta T = T_c - T = 1$ K, $\tau_\xi = 3.5$ µs as compared to $\tau_\xi = 4.5$ s for $\Delta T = 10^{-5}$ K. If one envisions that the forerunner shock wave rapidly compresses the test fluid to a near-critical state, the subsequent restoration of equilibrium must have a characteristic time of τ_ξ. Hence, we are led to believe that figure 18 (*c–g*) indeed shows transitory critical states. Note that there is a large increase in $\langle \Delta\rho^2 \rangle$, κ_T, c_p, and ξ when the vapour spinodal is approached, in a way very similar to the behaviour of the thermodynamic characteristics near the CP and thus referred to as the *pseudocritical* phenomena. The critical point is the limit of vapour–liquid equilibrium where the metastable and the unstable regions become one and the same. Phase transition is expected to proceed via similar mechanisms in the critical region and in the unstable region far from the CP. Consider figure 19 (*d–g*) and figure 21 which fit into the same framework described for complete liquefaction in §5.1; i.e. absence of a metastable state, formation of toroidal two-phase regions, and proximity to the VSP.

5.3. *Time delay of liquefaction*

The double pressure rise recorded by transducer T7 at the shock-tube endwall is surprisingly similar to the pressure records obtained in shock heating of a combustible gas and oxygen in a shock tube. In that case, a reflected shock heats the mixture with no reaction and the mixture ignites following an induction period, i.e. the so-called ignition delay time τ_i, which can be expressed as $\log \tau_i \propto 1/T_2$ (Lifshitz 1983). As can be seen in figure 24, the time delay between the consecutive pressure rises recorded by T7 displays a similar trend as a function of calculated T_2. Pressure records shown in figure 15 are typical of partial or complete liquefaction shocks when the R–H model does *not* predict a metastable state. The second rise is quite sharp and significant in magnitude (roughly 25% of the first rise) for a partial or complete LS. For strong shocks with $M_0 > 3$, the pressure signal shows large oscillations such that τ_i and the second jump become extremely hard to read from the signal. A satisfactory explanation for the intensity and delay of the second pressure rise has eluded us. We can only surmise that it is another manifestation of the phase decomposition in the unstable region. It is certainly possible that these pressure records and the corresponding photographed fluid states are tentative evidence for the 'sufficiently well-defined state' envisioned by Zeldovich (1981). This is a state immediately following a rapid transition in which short-range order is established, and the long-range fluctuations relax slowly.

6. Summary and conclusions

In recent shock-tube experiments, a liquefaction shock wave with a near critical downstream state is produced as a shock reflected from the endwall of the observation chamber. The following observations were consistently made for downstream states in the critical region:

On the liquid side: Sharply defined toroidal structures are observed with two-phase cores which grow and conglomerate to form larger two-phase structures, and, ultimately, a two-phase fog layer filling the shock tube (figure 17). These torus-form objects were first observed by Dettleff *et al.*, and there is ample reason to believe that these are vortex rings. Magnified images of these rings show a striking resemblance to the light-scattering rings observed in near-critical quenching of single-component fluids (figure 23).

Near the critical point: Circular two phase structures with diffuse boundaries are seen. Sometimes a torus shape is vaguely discernible; however, mostly smoke-like irregular fog regions are observed (figure 18).

On the vapour side: Two-phase structures with a striking resemblance to dandelions or orange slices are found (figure 19). Also, away from the critical region, circular two-phase structures with spikes emanating from the centre have been frequently observed.

These observations invariably correspond to the cases where the shock adiabat does not predict a metastable state and the (calculated) equilibrium downstream state (liquid or two-phase mixture) is in the critical region. Combined with the absence of a homogeneous fog layer filling the shock tube in the photographs, this suggests that the metastable region is passed without condensation via nucleation and growth. This possibility is supported by the estimates of the time- and lengthscales of the physical phenomena involved in the liquefaction-shock region. The leading shock wave is governed by the dissipative phenomena. The three molecular relaxation mechanisms (i.e. vibrational, rotational, and translational) are coupled. The estimated time for the fluid particle to pass the shock transition region, τ_{FS}, is of the order of 1 ns, which corresponds to a shock thickness, $\Delta_{FS} = O(0.01\ \mu\text{m})$. Critical clusters are nucleated within the shock zone while the fluid is supersaturated, i.e. $S = p_1/p_\infty(T_1) > 1$, where p_∞ is the vapour pressure. The maximum nucleation rate is estimated to reach high values, i.e. $J \sim 10^{30}\ \text{m}^{-3}\ \text{s}^{-1}$ based on a semiphenomenological droplet model. In the condensation relaxation zone, the phase transition is completed via further growth of the already nucleated clusters. Supersaturation returns back to unity while the nucleation of fresh clusters eventually ceases. This region has time- and lengthscales of $\tau_{CD} \sim 0.1$–$100\ \mu\text{s}$ and $\Delta_{CD} \sim 1$–$10^3\ \mu\text{m}$, respectively, decreasing with increasing shock strength. In complete shock liquefaction with near-critical end states, we can identify two different characteristic times. The short-range order (characteristic length δ) is established inside the LS front rapidly (10^{-11} s or maybe less). The long-range order (characteristic length ξ) is subsequently restored in a much longer time period which can be of the order of seconds very near the CP. Restoration of thermodynamic equilibrium near the CP is analogous to decomposition of a supersaturated fluid in the unstable region. Zeldovich (1981) refers to it as the re-establishment of the van der Waals (i.e. classical) critical point in a rapid process. It is certainly worth noting that this is very similar to the crossover from a rapid quench-depth-dependent rate of nucleation zone growth to a slower one observed by Goldburg & Huan (1975) in a critical binary mixture of 2–6 lutidine and water.

Vapour and liquid spinodals are lines connecting the extrema of cubic-shaped subcritical isotherms. From an empirical standpoint, a cubic-shaped isotherm is the simplest form to fit the experimentally determined stable and metastable states of a particular fluid. The cubic shape is also predicted by the van der Waals theory, which predicts a continuous transformation between liquid and vapour states. Thus, one can argue that the spinodal line, predicted by an empirical or theoretical state equation, is simply a mathematical limit which can never be established in real fluid flow experiments. Indeed, the vapour subcooling limit has been found to be quite far from the vapour spinodal whereas the liquid superheat is very close to the liquid spinodal. Zeldovich & Todes (see Skripov 1974) envisioned that in a rapid depressurization a liquid would decompose inside the unstable region, bypassing bubble nucleation and growth in the metastable region. However, liquid superheat experiments (pulse heating or nozzle expansion) typically have characteristic times of 1–10 μs, which are not short enough to hinder bubble nucleation before reaching the spinodal limit. The shock-tube experiments discussed herein differ from previous studies in two important respects; namely the timescale of the supersaturating flow regime ($O(1\text{ ns})$) and the direction of the flow (toward the spinodal and in the critical region). In comparison, cloud-chamber and nozzle experiments leading to condensation in regular fluids have timescales of the order of micro- and milliseconds at temperatures $T \leqslant 0.6T_c$, and they take the fluid away from the spinodal. We believe that there is sufficient experimental evidence to indicate that inside strong liquefaction shock waves with downstream states in the proximity of the vapour–liquid critical point, the phase transition mechanism is spinodal decomposition. This is also supported by estimates of physical parameters λ, δ, and r which are roughly of the same order of magnitude suggesting that, in a dense gas such as iso-octane, the phase transition is more continuous in nature than discrete. Away from the critical point, the metastable region the fluid has to pass through before reaching the spinodal is large such that the nucleation of clusters triggers the condensation onset well before the spinodal limit even within a short time. However, in the critical region the metastable region is smaller in scope, disappearing exactly at the critical point. A sufficiently rapid process such as a shock compression can then supersaturate the fluid such that nucleation is unable to initiate the condensation before the limit of (meta)stability. The phase transition is completed via a diffusion-dominated mechanism of simultaneous formation and growth of the interconnected regions of the new phase. Extreme shear rates inside the shock front lead to shear-layer instability and vortex roll-up at the phase interface. Thus, consistent observation of ring-shaped two-phase objects in reflected-liquefaction-shock experiments is thought to be a manifestation of spinodal decomposition in a single-component fluid.

This research was supported by NSF Grant MSM-881-15653 and partially by NSF Grant CTS-911-9468. The authors are indebted to J. E. Shepherd for his valuable suggestions.

REFERENCES

Cahn, J. W. 1968 Spinodal Decomposition. *Trans. AIME* **242**, 166–179.

Chen, G., Thompson, P. A. & Bursik, J. W. 1986 Soundspeed measurements in vapor-liquid mixtures behind shock waves. *Expts Fluids* **4**, 279–282.

Cho, H.-J. 1990 Experimental study of phase changes in isooctane in the general vicinity of the critical point. Dissertation, Rensselaer Polytechnic Institute.

Davies, L. & Wilson, J. L. 1969 Influence of reflected shock and boundary layer interaction in shock tube flows. *Phys. Fluids Suppl. I*, S37–43.

Delale, C. F. & Meier, G. E. A. 1993 A semiphenomenological droplet model of homogeneous nucleation from the vapor phase. *J. Chem. Phys.* **98**, 9850–9858.

Dettleff, G., Thompson, P. A., Meier, G. E. A. & Speckmann, H.-D. 1979 An experimental study of liquefaction shock waves. *J. Fluid Mech.* **95**, 279–304.

Dillmann, A. & Meier, G. E. A. 1991 A refined droplet approach to the problem of homogeneous nucleation from the vapor phase. *J. Chem. Phys.* **94**, 3872–3884.

Dremin, A. N. 1992 Shock discontinuity zone effect: the main factor in the explosive decomposition detonation process. *Phil. Trans. R. Soc. Lond.* A **339**, 355–364.

Feder, J., Russell, K. C., Lothe, J. & Pound, G. 1966 Homogeneous nucleation and growth of droplets in vapours. *Adv. Phys.* **15**, 111–178.

Goldburg, W. I. & Huang, J. S. 1975 Phase separation experiments near the critical point. In *Fluctuations, Instabilities, and Phase Transitions* (ed. Tormon Riste), pp. 87–106. Plenum.

Gülen, S. C. 1992 A study of shock splitting and liquefaction shocks in fast phase changes in retrograde fluids. Dissertation, Rensselaer Polytechnic Institute.

Gülen, S. C. 1993 A study of the liquefaction shock wave structure. *Phys. Fluids* (submitted).

Gülen, S. C. 1994 On the possibility of shock-induced condensation in the thermodynamically unstable region. *J. Non-Equilib. Thermodyn.* (to be published).

Hobbs, D. E. 1983 A virial equation of state utilizing the corresponding states principle. Dissertation, Rensselaer Polytechnic Institute.

Jany, P. 1988 Critical-point phenomena. In *Advanced Engineering Thermodynamics* (ed. A. Bejan), pp. 299–328. Wiley-Interscience.

Lifshitz, A. 1983 Anatomy of complex reaction systems; combustion reaction mechanisms from ignition delay times. In *Proc. 14th Intl Symp. on Shock Waves and Shock Tubes* (ed. R. D. Archer & B. E. Milton), pp. 26–40. New South Wales University Press, Sydney.

Passut, C. A. & Danner, R. P. 1972 Correlation of ideal gas enthalpy, heat capacity, and entropy. *Ind. Engng Chem. Process Des. Develop.* **11**, 543–546.

Reid, R. C., Prausnitz, J. M. & Poling, B. E. 1989 *The Properties of Gases & Liquids*, 4th Edn. McGraw Hill.

Schmitz, G., Klein, H. & Woermann, D. 1993 Gravity and shear flow effects on spinodal decomposition in single component fluids. *J. Chem. Phys.* **99**, 758–759.

Shepherd, J. E., Thompson, P. A. & Cho, H.-J. 1990 Alternating stability and instability of liquefaction shockfronts in 2,2,4-trimethylpentane. In *Proc. 17th Intl Symp. on Shock Waves and Shock Tubes* (ed. Y. W. Kim), pp. 790–795. AIP.

Skripov, V. P. 1974 *Metastable Liquids*, John Wiley & Sons.

Skripov, V. P. 1992 Metastable States. *J. Non-Equilib. Thermodyn.* **17**, 193–236.

Skripov, V. P. & Skripov, A. V. 1979 Spinodal decomposition (phase transitions via unstable states). *Sov. Phys. Usp.* **22**, 389–410.

Strehlow, R. A. & Cohen, A. 1958 Limitations of the reflected shock technique for studying fast chemical reactions and its application to the observation of relaxation in nitrogen and oxygen. *J. Chem. Phys.* **30**, 257–265.

Thompson, P. A., Carofano, G. C. & Kim, Y.-G. 1986 Shock waves and phase changes in a large-heat-capacity fluid emerging from a tube. *J. Fluid Mech.* **166**, 57–92.

Thompson, P. A., Chaves, H., Meier, G. E. A., Kim, Y.-G. & Speckmann, H.-D. 1987*a* Wave splitting in a fluid of large heat capacity. *J. Fluid Mech.* **185**, 385–414.

Thompson, P. A. & Kim, Y.-G. 1983 Direct observation of shock splitting in a vapor-liquid system. *Phys. Fluids* **26**, 3211–3215.

THOMPSON, P. A., KIM, Y.-G., YOON, C. J. & CHAN, Y. 1987*b* Nonequilibrium, near-critical states in shock tube experiments. In *Proc. 16th Intl Symp. on Shock Tubes and Waves* (ed. H. Grönig), pp. 343–349. VCH, Aachen.

THOMPSON, P. A. & SULLIVAN, D. A. 1975 On the possibility of complete condensation shock waves in retrograde fluids. *J. Fluid Mech.* **70**, 639–649.

TSONOPOULOS, C. 1974 An empirical correlation of second virial coefficients. *AIChE J.* **20**, 263–272.

WHITE, D. R. 1958 Influence of diaphragm opening time on shock tube flows. *J. Fluid Mech.* **4**, 585–600.

WU, B. J. C., WEGENER, P. P. & STEIN, G. D. 1977 Condensation of sulfurhexafluoride in steady supersonic nozzle flow. *J. Chem. Phys.* **68**, 308–318.

YOUNG, J. B. 1982 The spontaneous condensation of steam in supersonic nozzles. *Physiochem. Hydrodyn.* **3**, 57–82.

ZELDOVICH, YA. B. 1981 The reestablishment of the van der Waals critical point in fast processes. *Sov. Phys. JETP* **53**, 1101.